Computational Geosciences
https://doi.org/10.1007/s10596-019-9809-1

A nodal discontinuous Galerkin finite element method for the poroelastic wave equation

Khemraj Shukla[1] · **Jan S. Hesthaven**[2] · **José M. Carcione**[3] · **Ruichao Ye**[4] · **Josep de la Puente**[5] · **Priyank Jaiswal**[1]

Received: 25 July 2018 / Accepted: 28 January 2019

Abstract

We use the nodal discontinuous Galerkin method with a Lax-Friedrich flux to model the wave propagation in transversely isotropic and poroelastic media. The effect of dissipation due to global fluid flow causes a stiff relaxation term, which is incorporated in the numerical scheme through an operator splitting approach. The well-posedness of the poroelastic system is proved by adopting an approach based on characteristic variables. An error analysis for a plane wave propagating in poroelastic media shows a convergence rate of $O(h^{n+1})$. Computational experiments are shown for various combinations of homogeneous and heterogeneous poroelastic media.

Keywords Waves · Poroelasticity · Lax-Friedrich · Attenuation · Numerical flux

Mathematics Subject Classification (2010) 35L05 · 35S99 · 65M60 · 74J05 · 74J10 · 93C20

1 Introduction

The dynamics of fluid-saturated porous media is modeled by the poroelasticity theory, pioneered by Maurice Biot and presented in a series of seminal work during the 1930s to 1960s [11]. Porous media acoustics, modeling the propagation of waves in a porous media saturated with a fluid, is an important field of research in various science and engineering disciplines e.g., geophysics, soil mechanics, medical science, and civil engineering [1, 7]. In particular, in the exploration of oil and gas reservoirs, the quantitative estimation of porosity and permeability of rocks is very important to understand the direction of the fluid flow. In general, seismic modeling is performed by approximating the medium as a single phase (solid or fluid). These approximations are described by the acoustic [14, 18] and elastic [26, 32] rheologies and do not account for the loss of energy resulting from the fluid flow. To describe the wave propagation in the porous media, filled with a single phase fluid with an ability to flow through pore networks, Biot proposed the theory of poroelasticity [3–5].

✉ Khemraj Shukla
khemraj@okstate.edu

Extended author information available on the last page of the article.

Poroelasticity is a homogenized model of a porous medium, using linear elasticity (Hooke's law) to describe the solid (or skeleton) portion of the medium, linear compressible fluid dynamics to represent the fluid portion, and Darcy's law to model the flow through the pores. Thus, the poroelastic wave equation combines the constitutive relations with the equations of conservation of the momentum and Darcy's law. The global fluid flow results into the dissipation of energy due to the relative motion between the solid and fluid particles. Dissipation is incorporated in the equations of motion through a frequency dependent viscodynamic operator ($\psi(t)$). The behavior of the viscodynamic operator depends on the relaxation frequency (ω_c) [11] of the material. For frequencies lower than the relaxation frequency, $\psi(t)$ is independent of the frequency and compactly supported. In the high frequency range ($\geq \omega_c$), $\psi(t)$ becomes frequency dependent and incorporated in the equation of motion through convolution [9]. Our current work focuses on the poroleasticity in the low-frequency range ($< \omega_c$). This problem has already been solved by Carcione [9] using the pseudo-spectral method.

Unlike the acoustic and elastic approximations, wave propagation in a porous medium is a complex phenomenon. In poroelastic materials, three different types of waves appear: (1) a P wave, similar to an elastic P wave, with in-phase relative motion between the solid and the fluid; (2) a shear wave, similar to elastic S waves, and (3) a slow

Published online: 08 February 2019

P wave or Biot's mode with out-of-phase relative motion between the solid and the fluid. Dissipation of energy in the poroelastic system, caused by the relative motion between solid and fluid, causes very low attenuation (and velocity dispersion) in the low-frequency range for P and S waves whereas a very strong effect is seen in the slow P wave [8, 9, 11]. Thus, propagation of the slow P wave can be seen as a diffusion, which attenuates very rapidly. The slow P wave propagates at different time scales than those of the P and S waves, resulting in a stiff system of equations [8].

A wide variety of numerical methods have been used to solve the system of poroelastic wave equations. A detailed review is presented by Carcione et al. [10]. Most of the methods presented in this paper regard pseudo-spectral [8, 9], staggered pseudo-spectral [28], and finite-difference methods [15, 19] and are based on structured meshes. Santos and Oreña [31] used the finite-element method to solve the poroelastic wave equation using quadrilateral meshes for spatial discretization. Recent work on the numerical solution of orthotropic poroelasticity is reported by Lemoine et al. [25], using a finite-volume method on structured meshes. In our work, we develop a high-order discontinuous Galerkin (DG) method, which is well-suited for simulation of time-domain wave propagation, due to their low dispersion and the ability to accommodate unstructured meshes [20], unlike the finite-difference method.

The time-domain wave propagation, described by a hyperbolic system of partial differential equations, can be solved with an explicit time integration scheme if a stability condition is used on the time step length. In general, the finite-element method, coupled with explicit time integrator, requires the inversion of a global mass matrix. Spectral element methods avoids the inversion of the global mass matrix for hexahedral elements by choosing the nodal basis function, resulting in a diagonal mass matrix [24]. Inversion of the global mass matrix is avoided in the high-order DG method which produces locally invertible matrices. High-order DG methods are often used for seismic simulation (elastic approximation) through the use of simplicial meshes [12, 23, 35].

An inherent challenge in solving the poroelastic system is the treatment of the viscosity-dependent dissipation term. The poroelastic system of equations has the form $\dot{\mathbf{q}} = \mathbf{M}\mathbf{q}$, where $\mathbf{q}$ is the wave field vector and $\mathbf{M}$ is a propagation matrix. Since the system is dissipative, the eigenvalues of $\mathbf{M}$ will have a negative real part. The fastest wave in the system will have a small real part whereas the slowest mode (quasi-static) will have a large real part, making the differential equation stiff. The stiffness is more apparent in the low-frequency regime, whereas in the high frequency regime, separation between the time scales of the dissipation term and the wave motion is small. The stiffness can be handled in the the poroelastic system by using an implicit scheme for time integration but this will not be a computationally efficient approach. Nevertheless, the viscous term, responsible for the quasi-static mode, is easy to solve analytically, which makes operator splitting a natural choice to handle the stiffness. Carcione and Quiroga-Goode [8] solved the poroacoustic system with operator splitting paired with the pseudo-spectral method. The operator splitting approach in a DG method is also explored by de la Puente et al. [13] but to maintain the fast rate of convergence, they solved the system of low-frequency poroelastic wave equations (in stress-velocity form) in the diffusive limit by adopting a local space-time DG method [16]. The space-time DG method employs an expensive local implicit time integration scheme, based on the high-order derivatives (ADER) of the polynomial approximation functions. de la Puente et al. [13] also used a weak form of the numerical scheme in modal form, which requires smoothness on the test functions, generally suited for the non-linear conservation laws. However, the weak and strong, used in this work, formulations are mathematically equivalent but computationally very different.

In the same line of work, Dupuy et al. [17] solved the porolelastic wave equations in frequency domain using the discontinuous Galerkin method. The system of equation is solved for displacement field variables, expressed by a set of second order partial differential equations. Unlike the poroelastic model used in here, Dupuy et al. [17] used a frequency dependent permeability to deal with the entire frequency range in the numerical simulations. The rock physics model used by Dupuy et al. [17] closely follows the work of Pride [29]. Discontinuous Galerkin method used in [17] employs a central numerical flux. The central numerical flux is non-dissipative but makes the scheme unstable in heterogenous media. The stability and convergence of the numerical scheme is not discussed by Dupuy et al. [17]. The frequency-domain implementation circumvents the problem of stiffness implicitly but at the cost of solving the system at each frequency.

In another study, [33] solved the system of poroelastic wave equations, expressed in the strain-velocity formulation, using the upwind flux in an isotropic acoustic-poroelastic combination. In DG methods, the flux is applied at the shared edges of elements to recover the global solution. The application of upwind flux causes less dissipation but is more computer intensive as it requires an eigenvalue decomposition of Jacobian matrices. The eigenvalues and eigenvectors of the Jacobian, corresponding to a generic poroelastic medium is not trivial and poses a computational challenge. Furthermore, the upwind flux for an anisotropic medium requires the rotation of eigenvectors along normals of each edges of elements, although this can be avoided by using the Lax-Friedrich flux. To justify the choice of the Lax-Friedrich flux, we use the claim of Cockburn and Shu

[6], which states that the *particular choice of the flux does not play an important role for high-order simulations.* Furthermore, this claim is also substantiated for the poroelastic system. (discussed in Section 5.5).

In this work, we have used a Lax-Friedrich flux [21] which requires knowledge of the maximum speed present in the system to stabilize the numerical scheme. We used a plane-wave approach to compute the maximum speed. Unlike an upwind flux, Lax-Friedrich flux is very generic and can be extended from an isotropic to an anisotropic medium. We have used the 4th-order accurate low-storage explicit Runge-Kutta scheme for time integration of the non-dissipative (i.e, non-stiff part) part of the system. The novelties of our approach are (i) we use a coupled first-order low-frequency poroelastic wave equation in conservation form for a transversely anisotropic media. (ii) We prove well-posedness of the poroelastic system. In the usual sense, well-posedness of the system admits a unique solution of the system bounded in L^2 of the boundary or forcing data. (iii) We derive a self-consistent DG strong formulation with a Lax-Friedrich flux. (iv) We verify the method by comparing the analytical and numerical solutions. (v) We perform various computational experiments to study the slow P wave in isotropic and anisotropic media.

2 System of equations describing poroelastic wave equation in transversely isotropic medium

In this section, we discuss Biot's equations of poroelasticity but readers are advised to refer to Biot's original papers [3–5] and [11] for further detail.

2.1 Stress-strain relations

The constitutive equations for an inhomogeneous and transversely isotropic poroelastic media is expressed as [2, 9]

$$\partial_t \tau_{xx} = c^u_{11}\partial_x v_x + c^u_{13}\partial_z v_z + \alpha_1 M(\partial_x q_x + \partial_z q_z) + \partial_t s_{11}, \quad (1)$$

$$\partial_t \tau_{zz} = c^u_{13}\partial_x v_x + c^u_{33}\partial_z v_z + \alpha_3 M(\partial_x q_x + \partial_z q_z) + \partial_t s_{33}, \quad (2)$$

$$\partial_t \tau_{xz} = c^u_{55}(\partial_z v_x + \partial_x v_z) + \partial_t s_{55}, \quad (3)$$

$$\partial_t p = -\alpha_1 M \partial_x v_x - \alpha_3 M \partial_z v_z - M(\partial_x q_x + \partial_z q_z) + \partial_t s_f, \quad (4)$$

where τ_{xx}, τ_{zz}, and τ_{xz} are the total stresses, p is fluid pressure, the $v's$ and $q's$ are the solid and fluid (relative to solid) particle velocities, respectively, c^u_{ij}, $i, j = 1, ..., 6$ are the undrained components of the elastic stiffness tensor, M is an elastic modulus and α_k, $k = 1, 3$ are Biot's effective coefficients. s_{ij} and s_f are the solid and fluid forcing functions, respectively. The conventions are that ∂_t, ∂_x and ∂_z denote time derivative and spatial derivative operator in x and z directions, respectively. The basic underlying assumption in estimating the coefficients is that anisotropy of the porous solid frame is caused by the directional arrangement of the grains. The undrained coefficients c^u_{ij} are expressed in terms of drained coefficients, c_{ij}, as

$$c^u_{11} = c_{11} + \alpha_1^2 M, \quad (5)$$

$$c^u_{33} = c_{33} + \alpha_3^2 M, \quad (6)$$

$$c^u_{13} = c_{13} + \alpha_1 \alpha_3 M, \quad (7)$$

$$c^u_{55} = c_{55}. \quad (8)$$

Effective coefficients α and modulus M are given by [11]

$$\alpha_1 = 1 - \frac{c_{11} + c_{12} + c_{13}}{3K_s}, \quad (9)$$

$$\alpha_3 = 1 - \frac{2c_{13} + c_{33}}{3K_s}, \quad (10)$$

$$M = \frac{K_s^2}{D - (2c_{11} + c_{33} + 2c_{12} + 4c_{13})}, \quad (11)$$

where K_s is the bulk modulus of the grains and

$$D = Ks(1 - \phi + \phi K_s K_f^{-1}), \quad (12)$$

with K_f being the fluid bulk modulus and ϕ the porosity.

2.2 Dynamical equations and Darcy's law

The dynamic equations describing the wave propagation in a transversely isotropic heterogeneous porous medium, are given by [5, 11]

$$\partial_x \tau_{xx} + \partial_z \tau_{xz} = \rho \partial_t v_x + \rho_f \partial_t q_x, \quad (13)$$

$$\partial_x \tau_{xz} + \partial_z \tau_{zz} = \rho \partial_t v_z + \rho_f \partial_t q_z, \quad (14)$$

where $\rho = (1 - \phi)\rho_s + \phi\rho_f$ is the bulk density, and ρ_s and ρ_f are the solid and fluid density, respectively.

The generalized dynamic Darcy's law, governing the fluid flow in an anisotropic porous media, is expressed as [9]

$$-\partial_x p = \rho_f \partial_t v_x + \psi_1 * \partial_t q_x, \quad (15)$$

$$-\partial_z p = \rho_f \partial_t v_z + \psi_3 * \partial_t q_z, \quad (16)$$

where " $*$ " denotes the time convolution operators and ψ_i, i=1,3 are the time-dependent Biot's viscodynamic operator in the x and z directions. In the low-frequency range, i.e., for frequencies lower than $\omega_c = \min\left(\frac{\eta\phi}{\rho_f T_i \kappa_i}\right)$, ψ_i can be expressed as

$$\psi_i(t) = m_i \delta(t) + (\eta/\kappa_i) H(t), \quad (17)$$

where $m_i = T_i \rho_f / \phi$, with T_i being the tortuosity, η the fluid viscosity, and κ_1 and κ_3 the principal components of the global permeability tensor, while $\delta(t)$ is Dirac's function

and $H(t)$ the Heaviside step function. Substituting (17) in (15) and (16), we get

$$-\partial_x p = \rho_f \partial_t v_x + m_1 \partial_t q_x + \frac{\eta}{\kappa_1} q_x, \tag{18}$$

$$-\partial_z p = \rho_f \partial_t v_z + m_3 \partial_t q_z + \frac{\eta}{\kappa_1} q_z. \tag{19}$$

Equations (13), (14), (18), and (19) yield

$$\partial_t v_x = \beta_{11}^{(1)} (\partial_x \tau_{xx} + \partial_z \tau_{xz}) - \beta_{12}^{(1)} \left(\partial_x p + \frac{\eta}{\kappa_1} q_x \right), \tag{20}$$

$$\partial_t v_z = \beta_{11}^{(3)} (\partial_x \tau_{xz} + \partial_z \tau_{zz}) - \beta_{12}^{(3)} \left(\partial_z p + \frac{\eta}{\kappa_3} q_z \right), \tag{21}$$

$$\partial_t q_x = \beta_{21}^{(1)} (\partial_x \tau_{xx} + \partial_z \tau_{xz}) - \beta_{22}^{(1)} \left(\partial_x p + \frac{\eta}{\kappa_1} q_x \right), \tag{22}$$

$$\partial_t q_z = \beta_{21}^{(3)} (\partial_x \tau_{xz} + \partial_z \tau_{zz}) - \beta_{22}^{(3)} \left(\partial_z p + \frac{\eta}{\kappa_3} q_z \right), \tag{23}$$

where

$$\begin{bmatrix} \beta_{11}^{(k)} & \beta_{12}^{(k)} \\ \beta_{21}^{(k)} & \beta_{22}^{(k)} \end{bmatrix} = (\rho_f^2 - \rho m_k)^{-1} \begin{bmatrix} -m_k & \rho_f \\ \rho_f & -\rho \end{bmatrix}. \tag{24}$$

2.3 Equations in a system form

To simplify the notation, we introduce a system form of the equations by combining Eqs. (1)–(4) and (20)–(23). The conservation form of the system of poroelastic wave equations is

$$\partial_t \mathbf{q} + \nabla \cdot (\mathcal{A}\mathbf{q}) = \mathbf{D}\mathbf{q} + \mathbf{f}, \tag{25}$$

where $\mathbf{q} = [p\ \tau_{xx}\ \tau_{zz}\ \tau_{xz}\ v_x\ v_z\ q_x\ q_z]^T$, $\mathcal{A} = [\mathbf{A_1}\ \mathbf{A_2}\ \mathbf{A_3}]$ with

$$\mathbf{A_1} = \begin{bmatrix} 0 & 0 & 0 & 0 & \alpha_1 M & 0 & M & 0 \\ 0 & 0 & 0 & 0 & -c_{11}^u & 0 & -\alpha_1 M & 0 \\ 0 & 0 & 0 & 0 & -c_{13}^u & 0 & -\alpha_3 M & 0 \\ 0 & 0 & 0 & 0 & 0 & c_{55}^u & 0 & 0 \\ \beta_{12}^{(1)} & -\beta_{11}^{(1)} & 0 & 0 & 0 & 0 & 0 & 0 \\ 0 & 0 & 0 & -\beta_{11}^{(3)} & 0 & 0 & 0 & 0 \\ \beta_{22}^{(1)} & -\beta_{21}^{(1)} & 0 & 0 & 0 & 0 & 0 & 0 \\ 0 & 0 & 0 & -\beta_{21}^{(3)} & 0 & 0 & 0 & 0 \end{bmatrix}, \tag{26}$$

$$\mathbf{A_2} = \begin{bmatrix} 0 & 0 & 0 & 0 & 0 & \alpha_3 M & 0 & M \\ 0 & 0 & 0 & 0 & 0 & -c_{13}^u & 0 & -\alpha_1 M \\ 0 & 0 & 0 & 0 & 0 & -c_{33}^u & 0 & -\alpha_3 M \\ 0 & 0 & 0 & 0 & -c_{55}^u & 0 & 0 & 0 \\ 0 & 0 & 0 & -\beta_{11}^{(1)} & 0 & 0 & 0 & 0 \\ \beta_{12}^{(3)} & 0 & -\beta_{11}^{(3)} & 0 & 0 & 0 & 0 & 0 \\ 0 & 0 & 0 & -\beta_{21}^{(1)} & 0 & 0 & 0 & 0 \\ \beta_{22}^{3} & 0 & -\beta_{21}^{(3)} & 0 & 0 & 0 & 0 & 0 \end{bmatrix}, \tag{27}$$

$$\mathbf{D} = \begin{bmatrix} 0 & 0 & 0 & 0 & 0 & 0 & 0 & 0 \\ 0 & 0 & 0 & 0 & 0 & 0 & 0 & 0 \\ 0 & 0 & 0 & 0 & 0 & 0 & 0 & 0 \\ 0 & 0 & 0 & 0 & 0 & 0 & 0 & 0 \\ 0 & 0 & 0 & 0 & 0 & 0 & \frac{-\beta_{12}^{(1)}\eta}{\kappa_1} & 0 \\ 0 & 0 & 0 & 0 & 0 & 0 & 0 & \frac{-\beta_{12}^{(3)}\eta}{\kappa_3} \\ 0 & 0 & 0 & 0 & 0 & 0 & \frac{-\beta_{22}^{(1)}\eta}{\kappa_1} & 0 \\ 0 & 0 & 0 & 0 & 0 & 0 & 0 & \frac{-\beta_{22}^{(3)}\eta}{\kappa_3} \end{bmatrix}, \tag{28}$$

and $\mathbf{f} = [\partial_t s_{11}\ \partial_t s_{33}\ \partial_t s_{55}\ \partial_t s_f]^T$ is a forcing function. In this work, the forcing function is assumed to be the product of a compactly supported function in space (specifically Dirac delta function) and Ricker wavelet in the time domain.

3 Well-posedness of the poroelastic system of equations

In the velocity-stress formulation, the governing equations describing the wave propagation in a region Ω enclosed by its boundary $\partial\Omega$ and filled with heterogeneous transversely isotropic porous media, is expressed as

$$\begin{aligned} \mathbf{q}_t + \partial_x (\mathbf{A_1 q}) + \partial_z (\mathbf{A_2 q}) &= \mathbf{D}\mathbf{q} + \mathbf{f(t)}, \\ \mathbf{x} = (x, z) \in \Omega,\ t > 0, \\ \mathbf{q} = \mathbf{h(x)}, \quad \mathbf{x} \in \Omega,\ t = 0, \\ \mathcal{B}\mathbf{q} = \mathbf{g}(\mathbf{x}, t), \quad \mathbf{x} \in \partial\Omega,\ t \geq 0. \end{aligned} \tag{29}$$

To prove the well-posedness of the system (29), first, we seek a symmetrizer for $\mathbf{A_1}$ and $\mathbf{A_2}$.

The strain or potential energy of the poroelastic system is [11],

$$E_s = \frac{1}{2} \boldsymbol{\tau}^T \mathbf{C} \boldsymbol{\tau}, \tag{30}$$

where $\boldsymbol{\tau} = [\tau_{xx}\ \tau_{zz}\ \tau_{xz}\ p]^T$ and $\mathbf{C}$ is a symmetric undrained compliance matrix,

$$\mathbf{C} = \begin{bmatrix} C_{11} & C_{12} & 0 & C_{14} \\ C_{12} & C_{22} & 0 & C_{24} \\ 0 & 0 & C_{33} & 0 \\ C_{14} & C_{24} & 0 & C_{44} \end{bmatrix}, \tag{31}$$

where $C_{11} = \frac{c_{33}}{c_{11}c_{33}-c_{13}^2}$, $C_{12} = -\frac{c_{13}}{c_{11}c_{33}-c_{13}^2}$, $C_{14} = \frac{\alpha_1 c_{33}-\alpha_3 c_{13}}{c_{11}c_{33}-c_{13}^2}$, $C_{22} = \frac{c_{11}}{c_{11}c_{33}-c_{13}^2}$, $C_{24} = \frac{\alpha_3 c_{11}-\alpha_1 c_{13}}{c_{11}c_{33}-c_{13}^2}$, $C_{33} = \frac{1}{c_{55}}$, $C_{44} = \frac{\alpha_3 c_{11}-\alpha_1 c_{13}}{c_{11}c_{33}-c_{13}^2}$.

The kinetic energy of the poroelastic system can be written as [11]

$$E_v = \frac{1}{2}\left[\rho \mathbf{v}^T\mathbf{v} + 2\rho_f \mathbf{q}^T\mathbf{v} + \mathbf{q_f}^T\mathbf{m}\mathbf{q_f}\right], \tag{32}$$

where $\mathbf{v} = [v_x\ v_z]^T$, $\mathbf{q_f} = [q_x\ q_z]^T$ and $\mathbf{m} = \begin{pmatrix} m_1 & 0 \\ 0 & m_3 \end{pmatrix}$. To construct a simultaneous symmetrizer ($\mathcal{H}$, a symmetric positive definite operator) for Jacobians $\mathbf{A_1}$ and $\mathbf{A_2}$, a block-diagonal matrix with non-zero elements, being the Hessian of (30) and (32), is expressed as

$$\mathcal{H} = \begin{bmatrix} \mathbf{E}_{11} & 0 \\ 0 & \mathbf{E}_{22} \end{bmatrix}, \tag{33}$$

where $E_{11} = \text{Hessian}(E_s) = \Delta E_s(p\ \tau_{xx}\ \tau_{zz}\ \tau_{xz})$ and $E_{22} = \text{Hessian}(E_v) = \Delta E_s(v_x\ v_z\ q_x\ q_z)$. Hence $\mathbf{E}_{11}$.

$$\mathbf{E}_{11} = \begin{bmatrix} e_{11} & e_{12} & e_{13} & 0 \\ e_{21} & e_{22} & e_{23} & 0 \\ e_{13} & e_{23} & e_{33} & 0 \\ 0 & 0 & 0 & e_{44} \end{bmatrix}$$

and

$$\mathbf{E}_{22} = \begin{bmatrix} \rho & 0 & \rho_f & 0 \\ 0 & \rho & 0 & \rho_f \\ \rho_f & 0 & m_1 & 0 \\ 0 & \rho_f & 0 & m_3 \end{bmatrix},$$

where $e_{11} = \frac{\alpha_1^3 c_{33} + \alpha_3^2 c_{11} - 2\alpha_1\alpha_3 c_{13}}{c_{11}c_{33}-c_{13}^2} + \frac{1}{M}$, $e_{12} = \frac{\alpha_1 c_{33}-\alpha_3 c_{13}}{c_{11}c_{33}-c_{13}^2}$, $e_{13} = \frac{\alpha_3 c_{11}-\alpha_1 c_{13}}{c_{11}c_{33}-c_{13}^2}$, $e_{22} = \frac{c_{33}}{c_{11}c_{33}-c_{13}^2}$, $e_{23} = -\frac{c_{13}}{c_{11}c_{33}-c_{13}^2}$, $e_{33} = -\frac{c_{13}}{c_{11}c_{33}-c_{13}^2}$ and $e_{44} = \frac{1}{c_{55}}$.

Applying $\mathcal{H}$ to $\mathbf{A_1}$, $\mathbf{A_2}$ and $\mathbf{D}$ yields

$$\mathcal{H}\mathbf{A_1} = \widetilde{\mathbf{A}}_1 = \begin{bmatrix} 0&0&0&0&0&0&1&0 \\ 0&0&0&0&-1&0&0&0 \\ 0&0&0&0&0&0&0&0 \\ 0&0&0&0&0&-1&0&0 \\ 0&-1&0&0&0&0&0&0 \\ 0&0&0&-1&0&0&0&0 \\ 1&0&0&0&0&0&0&0 \\ 0&0&0&0&0&0&0&0 \end{bmatrix}, \tag{34}$$

$$\mathcal{H}\mathbf{A_2} = \widetilde{\mathbf{A}}_2 = \begin{bmatrix} 0&0&0&0&0&0&0&1 \\ 0&0&0&0&0&0&0&0 \\ 0&0&0&0&0&-1&0&0 \\ 0&0&0&0&-1&0&0&0 \\ 0&0&0&-1&0&0&0&0 \\ 0&0&-1&0&0&0&0&0 \\ 0&0&0&0&0&0&0&0 \\ 1&0&0&0&0&0&0&0 \end{bmatrix}, \tag{35}$$

$$\mathcal{H}\mathbf{D} = \widetilde{\mathbf{D}} = \begin{bmatrix} 0&0&0&0&0&0&0&0 \\ 0&0&0&0&0&0&0&0 \\ 0&0&0&0&0&0&0&0 \\ 0&0&0&0&0&0&0&0 \\ 0&0&0&0&0&0&0&0 \\ 0&0&0&0&0&0&0&0 \\ 0&0&0&0&0&-\frac{\eta}{\kappa_1}&0 \\ 0&0&0&0&0&0&-\frac{\eta}{\kappa_3} \end{bmatrix}, \tag{36}$$

where $\widetilde{\mathbf{A}}_1$ and $\widetilde{\mathbf{A}}_2$ are symmetric and $\widetilde{\mathbf{D}}$ is a negative semi-definite matrix. $\mathcal{H}$ is positive-definite and symmetrizes $\mathbf{A}_1$ and $\mathbf{A}_2$. Thus well-posedness of (29) follows by energy estimate $E(t)$, which is expressed as

$$E(t) = \frac{1}{2}\mathbf{q}^T\mathcal{H}\mathbf{q}. \tag{37}$$

It suffices to consider (29) for $\eta = 0$ and $\mathbf{f} = \mathbf{0}$. Multiplying (29) with $\mathbf{q^T}\mathcal{H}$, integrating over Ω and using the divergence theorem, we recover,

$$\frac{dE(t)}{dt} = \oint_{\partial\Omega} \mathbf{q^T}\mathbf{A(n)}\mathbf{q}\, d\mathbf{x}, \tag{38}$$

where $\oint_{\partial\Omega}$ denotes the line integral over $\partial\Omega$ and

$$\mathbf{A(n)} = \sum_{i=1}^{2} n_i \widetilde{\mathbf{A}}_i = \begin{bmatrix} 0&0&0&0&0&0&n_1&n_2 \\ 0&0&0&0&-n_1&0&0&0 \\ 0&0&0&0&0&-n_2&0&0 \\ 0&0&0&0&-n_2&-n_1&0&0 \\ 0&-n_1&0&-n_2&0&0&0&0 \\ 0&0&-n_2&-n_1&0&0&0&0 \\ n_1&0&0&0&0&0&0&0 \\ n_2&0&0&0&0&0&0&0 \end{bmatrix}.$$

Since $\mathbf{A(n)}$ is symmetric, there exists an unitary matrix $\mathbf{S(n)}$ such that $\mathbf{A(n)} = \mathbf{S(n)}^\mathbf{T}\Lambda\mathbf{S(n)}$. The expression for $\mathbf{S}$ and Λ are given as

$$\mathbf{S(n)} = \begin{bmatrix} 0&0&-\frac{1}{n_2}&\frac{1}{n_2}&0&0&0&0 \\ 0&-\frac{n_2}{n_1}&0&0&-\frac{n_1}{\alpha_-}&\frac{n_1}{\alpha_-}&\frac{n_1}{\alpha_+}&-\frac{n_1}{\alpha_+} \\ 0&-\frac{n_1}{n_2}&0&0&\frac{\alpha_-}{n_2}&-\frac{\alpha_-}{n_2}&\frac{\alpha_+}{n_2}&-\frac{\alpha_+}{n_2} \\ 0&1&0&0&-\frac{-n_1+n_2}{\alpha_-}&-\frac{\alpha_-}{n_1-n_2}&\frac{\alpha_+}{-n_1-n_2}&-\frac{\alpha_+}{n_1+n_2} \\ 0&0&0&0&-1&-1&1&1 \\ 0&0&0&0&1&1&1&1 \\ -\frac{n_2}{n_1}&0&\frac{n_1}{n_2}&\frac{n_1}{n_2}&0&0&0&0 \\ 1&0&1&1&0&0&0&0 \end{bmatrix},$$

where $\Lambda = \mathbf{diag}\left[\lambda_1\ \lambda_2\ \lambda_3\ \lambda_4\ \lambda_5\ \lambda_6\ \lambda_7\ \lambda_8\right]$

$= \mathbf{diag}\left[0\ 0 - 1\ 1\ -\alpha_-\ \alpha_-\ -\alpha_+\ \alpha_+\right]$ with

$\alpha_\pm = \sqrt{1 \pm n_1 n_2}$.

The characteristic state vector $\mathbf{R}$ is expressed as

$$\mathbf{R(n)} = \mathbf{S^T(n)q} = [R_1, R_2, R_3, R_4, R_5, R_6, R_7, R_8]^T \ . \quad (39)$$

Thus we have

$$\mathbf{q}^T \mathbf{A(n)q} = \mathbf{R}^T \Lambda(n)\mathbf{R(n)} = \sum_{i=1}^{8} (\lambda_i R_i^2). \quad (40)$$

Substituting (40) in (38), we recover

$$\frac{dE(t)}{dt} = \sum_{i=1}^{8} IS_i, \quad IS_i = \oint_{\partial\Omega} (\lambda_i R_i^2)\, d\mathbf{x}. \quad (41)$$

Equation (41) implies that the net rate of change of the energy with respect to time is estimated by summing the surface integrals. Surface integrals for $i = 4, 6, 8$ contribute to the energy of the system from the boundary. Surface integrals for $i = 3, 5, 7$ extract out the energy from the system, if the integral is not zero. Thus R_4, R_6, R_8 are incoming characteristics and R_3, R_5, R_7 are outgoing characteristics. For $\lambda_1 = \lambda_2 = 0$ there is no addition or subtraction of energy to the system thus, characteristic variables R_1, R_2 are stationary characteristics. Since $\lambda_3, \lambda_5,$ and λ_7 are negative,

$$\frac{dE(t)}{dt} \leq \oint_{\partial\Omega} (R_4^2 + \alpha_- R_6^2 + \alpha_+ R_8^2)\, d\mathbf{x}, \quad (42)$$

which implies that if a boundary condition is of the form

$$\mathcal{B}\mathbf{q} = \begin{bmatrix} \mathbf{s}_4^T \\ \mathbf{s}_6^T \\ \mathbf{s}_8^T \end{bmatrix} \mathbf{q} = \mathbf{g}(\mathbf{x}, t) = \begin{bmatrix} \mathbf{g}_1(\mathbf{x}, t) \\ \mathbf{g}_2(\mathbf{x}, t) \\ \mathbf{g}_3(\mathbf{x}, t) \end{bmatrix} \text{ and } \mathbf{x} \in \partial\Omega \ , \quad (43)$$

and we have

$$\begin{aligned} &\oint_{\partial\Omega} (R_4^2 + \alpha_- R_6^2 + \alpha_+ R_8^2) \\ &\leq \max(1, \alpha_-, \alpha_+) \Big(\oint_{\partial\Omega} \mathbf{q}^T \mathbf{s_4 s_4}^T \mathbf{q} d\mathbf{x} \\ &\quad + \oint_{\partial\Omega} \mathbf{q}^T \mathbf{s_6 s_6}^T \mathbf{q} d\mathbf{x} + \oint_{\partial\Omega} \mathbf{q}^T \mathbf{s_8 s_8}^T \mathbf{q} d\mathbf{x} \Big) \\ &= \alpha \oint_{\partial\Omega} |\mathbf{g}(\mathbf{x}, t)|^2 \, d\mathbf{x} = \alpha G(t), \\ &\quad \text{with } \alpha = \max(1, \alpha_-, \alpha_+). \end{aligned}$$

Thus we recover

$$\frac{dE(t)}{dt} \leq G(t).$$

Integrating w.r.t. time yields

$$E(t) \leq \int_0^t G(\chi) d\chi + E(0) \leq E(0) + t \max_{\chi \in [0,t]} G(\chi).$$

Alternatively,

$$\int_\Omega \mathbf{q^T}(\mathbf{x}, t)\mathbf{Hq}(\mathbf{x}, t)\, d\mathbf{x} \leq \int_{\partial\Omega} \mathbf{h}^T(\mathbf{x})\mathbf{Hh}(\mathbf{x}) d\mathbf{x} + t \left(\max_{\chi \in [0,t]} G(\chi) \right). \quad (44)$$

Equation (44) states that the energy of the system is bounded by the initial condition $\mathbf{h}(\mathbf{x}, t)$ and the boundary condition $\mathbf{g}(\mathbf{x}, t)$, prescribed by (29). Thus, the poroelastic system of equation, defined by Eq. (29), is a well-posed problem. This result is summarized in the theorem.

Theorem 1 *Assume there exist a smooth solution to* (29). *If the boundary condition is given of the form*

$$\mathcal{B}\mathbf{q} = \begin{bmatrix} \mathbf{s}_4^T \\ \mathbf{s}_6^T \\ \mathbf{s}_8^T \end{bmatrix} \mathbf{q} = \mathbf{g}(\mathbf{x}, t) = \begin{bmatrix} \mathbf{g}_1(\mathbf{x}, t) \\ \mathbf{g}_2(\mathbf{x}, t) \\ \mathbf{g}_3(\mathbf{x}, t) \end{bmatrix} \text{ and } \mathbf{x} \in \partial\Omega \ ,$$

then the IBVP (29) is well-posed and $\mathbf{q}$ *satisfies the estimate*

$$\int_\Omega \mathbf{q^T}(t)\mathbf{Hq}(t) d\mathbf{x} \leq \int \mathbf{h}^T(\mathbf{x})\mathbf{Hh}(\mathbf{x}) d\mathbf{x} + t \max_{\chi \in [0,t]} G(\chi),$$

with

$$G(t) = \alpha \oint_{\partial\Omega} |\mathbf{g}(\mathbf{x}, \mathbf{t})|^2 d\mathbf{x}, \quad \alpha = \max_{\mathbf{x} \in \partial\Omega} (1, \alpha_+, \alpha_-). \quad (45)$$

4 Numerical scheme

In absence of a forcing function, the poroelastic system of Eq. (25) can be expressed as

$$\mathbf{q_t} = \mathbf{Mq}, \quad (46)$$

where $\mathbf{M}$ is the propagator matrix, containing the material properties and spatial derivative operators. The eigenvalues of $\mathbf{M}$ come in conjugate pairs. For an inviscid pore fluid ($\eta = 0$), the eigenvalues of $\mathbf{M}$ lie along the imaginary axis, which implies the absence of dissipation from the system. On the other hand, for the viscous pore fluid ($\eta \neq 0$), the eigenvalues of $\mathbf{M}$ also contain a negative real part. Furthermore, a substantial difference between the magnitude of the real part of eigenvalues of different wave modes in the system causes it to be stiff. Figure 1 shows the representative eigenvalues of (46) computed for an isotropic sandstone with material properties given in Table 1. Stiffness in the system causes instabilities in explicit time integration schemes unless a very small time step is used. Alternatively, an implicit time integration scheme can be an unconditionally stable, but not efficient for a linear hyperbolic system. Carcione and co-workers have used an explicit approach in time operator splitting, also known as Godunov splitting or fractional step [8, 9, 11], which separates the dissipative term from the conservation

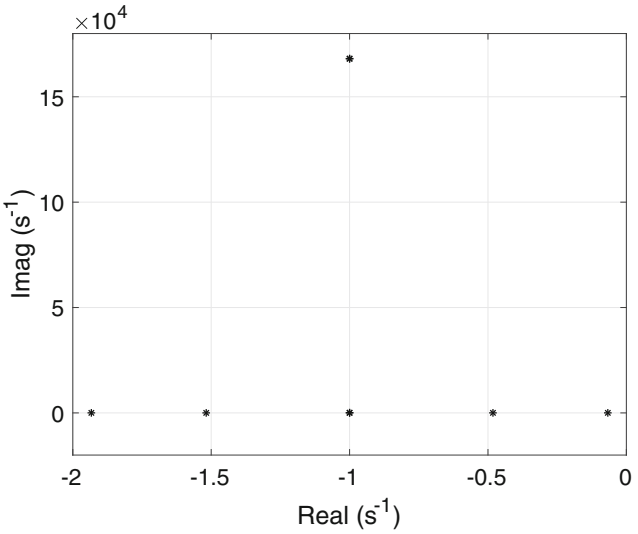

Fig. 1 Eigenvalues of the propagator matrix **M** at 22 Hz

term at each time step. In our work, we solve the stiff (dissipative) part of the system analytically and the non-stiff (conservation) part by using a nodal DG method, paired with a 4th-order low-storage explicit Runge-Kutta scheme (LSERK) [21]. Equation (25) is split into stiff and non-stiff part as follows: stiff part:

$$\partial_t \mathbf{q} = \mathbf{D}\mathbf{q}. \tag{47}$$

Non-stiff part:

$$\partial_t \mathbf{q} + \nabla \cdot (\mathcal{A}\mathbf{q}) = \mathbf{f}. \tag{48}$$

At each time step, Eq. (47), which is a simple ordinary differential equation, is solved analytically [9] and these intermediate solutions are plugged into (48) as an initial solution. The analytical solution of Eq. (47) is given in Appendix A. The numerical solution of (48) is computed using the nodal DG finite-element method, discussed next.

Table 1 Material properties for sandstone saturated with brine [8]

Properties	Sandstone (Isotropic)
K_s (GPa)	40
ρ_s (kg/m^3)	2500
ϕ	0.2
κ (10^{-15} m^2)	600
K_f (GPa)	2.5
ρ_f (kg/m^3)	1040
T_1	3
T_3	3
η (10^{-3} Kg/m.s)	1
λ^* (m/s)	3800

*Computed in this study

4.1 Nodal discontinuous Galerkin scheme for the poroelastic system

We consider that the domain Ω is Lipschitz and triangulated by D^k elements, where each element D^k is the image of a reference element $\hat{D}$ under the local mapping

$$\mathbf{x^k} = \Phi\hat{\mathbf{x}}, \tag{49}$$

where $\mathbf{x^k}$ and $\hat{\mathbf{x}}$ denote the physical and reference coordinates on D^k and $\hat{D}$, respectively. The approximate local solution over each element is expressed as

$$V_h(D^k) = \Phi^k \circ V_h(\hat{D}), \tag{50}$$

where $V_h(D^k)$ and $V_h(\hat{D})$ represent the approximation spaces for the physical and the reference element, respectively.

The global solution space $V_h(\Omega_h)$ is defined as the direct sum of the local approximation spaces

$$V_h(\Omega_h) = \bigoplus_{D^k} V_h(D^k). \tag{51}$$

In this work, we take $V_h(\hat{D}) = P^N(\hat{D})$, where $P^N(\hat{D})$ is the polynomial space of total degree N on the reference element.

Let f be the face of element D^k with neighboring element $D^{k,+}$ and unit outward normal vector $\mathbf{n}$. Let u be a function which is discontinuous across the element interface. The interior value u^- and exterior value u^+ on a face f of D^k are defined as

$$u^- = u|_{f \bigcap \partial D^k}, \quad u^+ = u|_{f \bigcap \partial D^{k,+}}.$$

Jump and average of a scalar function u over f is defined as

$$[\![u]\!] = u^+ - u^-, \qquad \{\!\{u\}\!\} = \frac{u^+ + u^-}{2}. \tag{52}$$

The jump and average of a vector valued functions are computed component wise.

The nodal DG scheme for (48) can be constructed by multiplying (48) with a basis function $\mathbf{p} \in P^N(\hat{D})$ and integrating by parts twice

$$\begin{aligned} &\int_{D^k} \left(\partial_t \mathbf{q_h} + \nabla \cdot (\mathcal{A}\mathbf{q_h})\right) \cdot \mathbf{p}\, d\mathbf{x} \\ &+ \int_{\partial D^k} ((\mathcal{A}_n \mathbf{q_h})^* - (\mathcal{A}_n \mathbf{q_h})^-) \cdot \mathbf{p}\, d\mathbf{x} \\ &= \int_{D^k} \mathbf{f} \cdot \mathbf{p}\, d\mathbf{x}, \end{aligned} \tag{53}$$

where $\mathbf{q_h}$ is the discretized solution, ($\mathcal{A}_n$ is the normal matrix defined on face f as $\mathcal{A}_n = n_1 A_1 + n_2 A_2$ and $(\mathcal{A}_n \mathbf{q_h})^*$ represents the numerical flux. Equation (53) represents the numerical scheme in strong form [21, p. 22] and thus does not require any smoothness on the basis function $\mathbf{p}$. To compute the basis function $\mathbf{p}$, we have

utilized the nodal basis function approach, discussed in the following section.

4.2 Nodal basis function

The discretized solution $\mathbf{q_h}$ in (48) follows a component-wise expansion into $N_p = N_{dof}^{D^k} = N_{dof}^{D^k}(N)$ nodal trial basis function of order N [21],

$$\mathbf{q_h}(\mathbf{x}, t) = \bigoplus_{D^k} \sum_{n=1}^{N_p} \mathbf{q_{h,n}^{D^k}}(t)\, p_n(\mathbf{x}). \tag{54}$$

Here $\mathbf{q_{h,n}^{D^k}}$ indicates the local expansion of $\mathbf{q_h}$ within element D^k, $p_n(\mathbf{x})$ is a set of 2-D Lagrange polynomials associated with the nodal points, $\{x_n\}_{n=1}^{N_p}$. The explicit expression for computing the Lagrange polynomials in 2D space is not known, but can be constructed by expressing the approximated solution in modal and nodal form, simultaneously. Expressing the $\mathbf{q_{h,n}^{D^k}}$ in modal and nodal form simultaneously, yields

$$\mathcal{V}^T p_n(\mathbf{x}) = \mathbf{P_n}(\mathbf{x}), \tag{55}$$

where $\mathcal{V}$ is the Vandermonde matrix of basis functions, used for approximating the modal form $\mathbf{q_{h,n}^{D^k}}$ and $\mathbf{P_n}(\mathbf{x})$ is a 2D orthonormalized basis function, constructed from Jacobi polynomials.

We have used the warp and blend method [21] to determine the coordinates of the nodal points in a triangle; for order N interpolation, there are $N_p = \frac{(N+1)(N+2)}{2}$ such nodes.

4.3 Numerical flux

The numerical flux $(\mathcal{A}_n q_h)^*$ in (53) determines the unique solution at the shared edges of two elements. In this paper, we use the Lax-Friedrich flux [27] to compute $(\mathcal{A}_n q_h)^*$. The Lax-Friedrich flux is expressed as

$$(\mathcal{A}_n q_h)^* = \{\{\mathcal{A}_n q_h\}\} + \frac{\lambda}{2}[\![q_h]\!], \tag{56}$$

where λ is the maximum speed of the waves in the system. Substituting (56) into (53) and using the identities in (52), we recover the local strong form of the semi-discrete DG scheme as

$$\begin{aligned} &\int_{D^k} \left(\partial_t \mathbf{q_h} + \nabla \cdot (\mathcal{A}_n \mathbf{q_h})\right) \cdot \mathbf{p}\, d\mathbf{x} \\ &+ \int_{\partial D^k} \left([\![\mathcal{A}_n \mathbf{q_h}]\!] + \frac{\lambda}{2}[\![\mathbf{q_h}]\!]\right) \cdot \mathbf{p}\, d\mathbf{x} \\ &= \int_{D^k} \mathbf{f} \cdot\ \mathbf{p}\, d\mathbf{x}. \end{aligned} \tag{57}$$

The global representation of (57) is obtained by summing the local form of the semi-discrete DG scheme over all the elements in Ω_h, expressed as

$$\begin{aligned} &\sum_{D^k \in \Omega_h} \left(\int_{D^k} \left(\partial_t \mathbf{q_h} + \nabla \cdot (\mathcal{A}_n \mathbf{q_h})\right) \cdot \mathbf{p}\, d\mathbf{x}\right) \\ &+ \int_{\partial D^k} \left([\![\mathcal{A}_n \mathbf{q_h}]\!] + \frac{\lambda}{2}[\![\mathbf{q_h}]\!]\right) \cdot \mathbf{p}\, d\mathbf{x} \\ &= \sum_{D^k \in \Omega_h} \left(\int_{D^k} \mathbf{f} \cdot\ \mathbf{p}\, d\mathbf{x})\right). \end{aligned} \tag{58}$$

In order to compute λ, the maximum speed of the wave in the system, we have used a plane-wave approach [9]. A detailed formulation for computing λ is given in Appendix B.

4.4 Boundary conditions

The top surface of the domain is modeled as a free surface by assuming that stress components and pore-fluid pressure is zero,

$$p = 0, \quad \sigma_{xx} = 0, \quad \tau_{zz}, \quad \tau_{xz} = 0. \tag{59}$$

The free surface boundary conditions are imposed by computing the numerical flux by modifying the jump in stress variables, for example, the modified jump in variable τ_{xx} is expressed as

$$[\![\tau_{xx}]\!] = -2\tau_{xx}^{-}. \tag{60}$$

The other boundaries are modeled as absorbing boundaries. The absorbing boundaries are implemented as outflow boundaries by setting the flux (at the boundaries) equal to zero. We note that more accurate absorbing conditions can be also imposed, for example perfectly matched layers [36] but these implementation always come with the added computational cost.

4.5 Time discretization

In the present study, we have employed the low-storage explicit Runge-Kutta (LSERK) method [6]. The LSERK method is a single-step method but comprises of five intermediate stages. LSERK is preferred over other methods as it saves memory at the cost of computation time. A stable CFL condition depending on the polynomial degree N is derived by Cockburn and Shu [6] and employed here.

4.6 Variational crime

In many applications, the external forcing function $\mathbf{f}$ is considered as a point source or Dirac function. A Dirac delta

function is not L^2 integrable and the term $\int_{D^k} \mathbf{f} \cdot \mathbf{p}\, d\mathbf{x}$ in (57) may not well defined. Thus, we commit a variational crime while evaluating the $\mathbf{f}(\mathbf{x}) = \delta(\mathbf{x} - \mathbf{x_0})$. A point source approximation is numerically implemented as

$$\sum_{D^k} \int_{D^k} \delta(\mathbf{x} - \mathbf{x_0}) \cdot \mathbf{p} = \int_{\Omega} \mathbf{p} \cdot \delta(\mathbf{x} - \mathbf{x_0}) = \mathbf{p}(\mathbf{x_0}).$$

5 Computational experiments

In this section, we illustrate the accuracy of our numerical scheme by comparing the analytical solution with the numerical solution and investigate the convergence. To check the accuracy between the numerical and the analytical solutions, we started our computational experiments with a poroacoustic system [8], which is a simplified poroelastic system, obtained by setting the solid rigidity to zero. Thus poroacoustic simulation only models the dilatational deformation. The properties of a poroacoustic media have been used to to describe the kinematics of emulsions and gels [22]. A system of equations describing the poroacoustic wave equation is given in Appendix C.

5.1 Poroacoustic medium: comparison of analytical and numerical solutions

The analytical solution of a point source in a 2D homogeneous poroacoustic medium is given by Carcione and Quiroga-Goode [8] and implemented here to evaluate the quality of the solution obtained from our nodal DG scheme. The forcing function **f** is the product of Dirac's delta in space and Ricker's wavelet in time, which is expressed as

$$f(t) = \exp\left[-\frac{1}{2} f_c^2 (t - t_0)^2\right] \cos[\pi f_c (t - t_0)], \tag{61}$$

where f_c is the source central frequency of the source and $t_0 = 3/f_c$ is the wavelet delay.

Figure 2a and b present a comparison between the analytical and the numerical solutions of the bulk and the

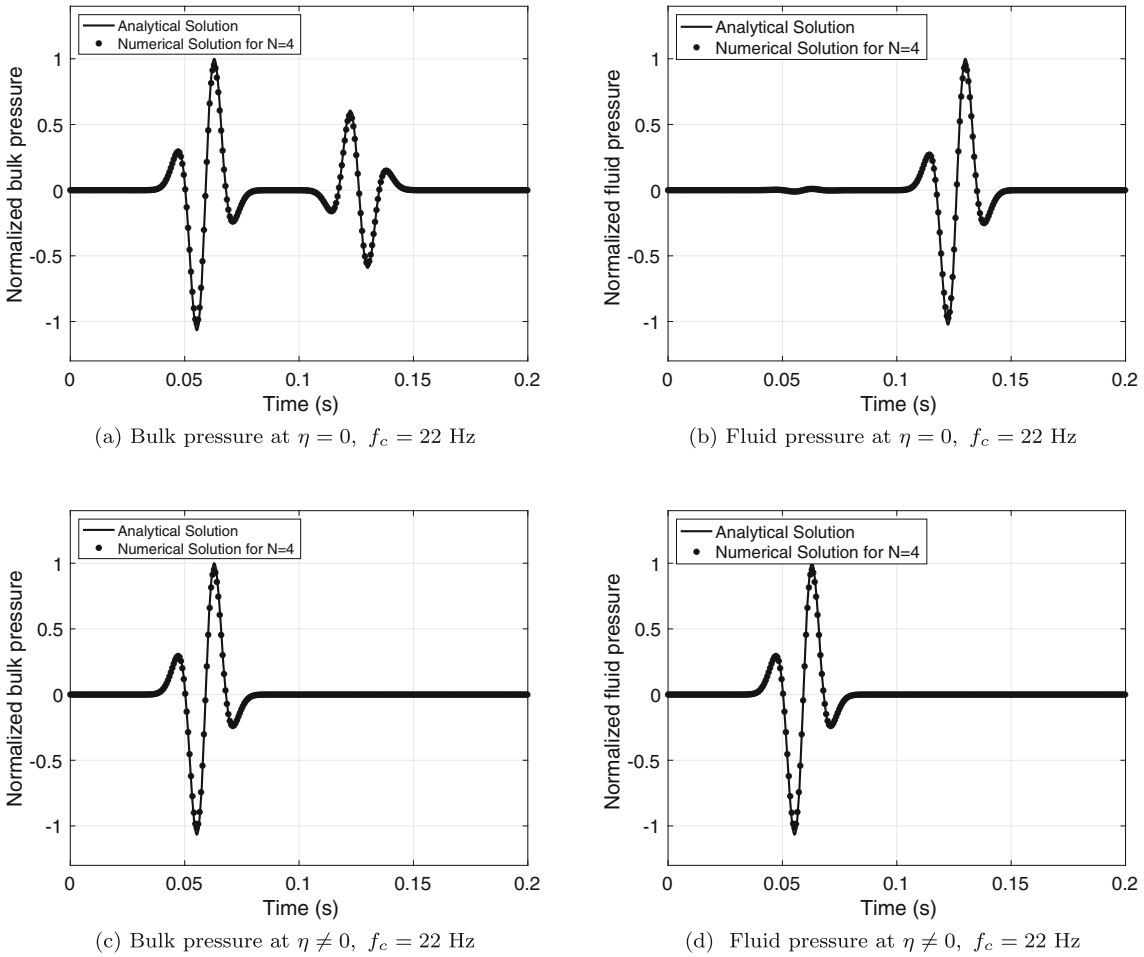

(a) Bulk pressure at $\eta = 0,\ f_c = 22$ Hz

(b) Fluid pressure at $\eta = 0,\ f_c = 22$ Hz

(c) Bulk pressure at $\eta \neq 0,\ f_c = 22$ Hz

(d) Fluid pressure at $\eta \neq 0,\ f_c = 22$ Hz

Fig. 2 A comparison between the analytical and the numerical solutions, computed in a poroacoustic media, at source-receiver offset of 250 m, and $f_c = 22\ Hz$, where **a** normalized bulk pressure ($\eta = 0$), **b** normalized fluid pressure, computed with ($\eta = 0$), **c** normalized bulk pressure ($\eta \neq 0$), and **d** normalized fluid pressure, computed with ($\eta \neq 0$)

Table 2 Material properties for several poroelastic media used in the examples [9, 13]

Properties	Sandstone (Orthotropic)	Epoxy-glass (Orthotropic)	Sandstone (Isotropic)	Shale (Isotropic)
K_s (GPa)	80	40	40	7.6
ρ_s (kg/m^3)	2500	1815	2500	2210
c_{11} (GPa)	71.8	39.4	36	11.9
c_{12} (GPa)	3.2	1.2	12	3.96
c_{13} (GPa)	1.2	1.2	12	3.96
c_{33} (GPa)	53.4	13.1	36	11.9
c_{55} (GPa)	26.1	3	12	3.96
ϕ	0.2	0.2	0.2	0.16
v κ_1 (10^{-15} m^2)	600	600	600	100
κ_3 (10^{-15} m^2)	100	100	600	100
T_1	2	2	2	2
T_3	3.6	3.6	2	2
K_f (GPa)	2.5	2.5	2.5	2.5
ρ_f (Kg/m^3)	1040	1040	1040	1040
η (10^{-3} Kg/m.s)	1	1	1	1
λ^* (m/s)	6000	5240	4250	2480

*Computed in this study

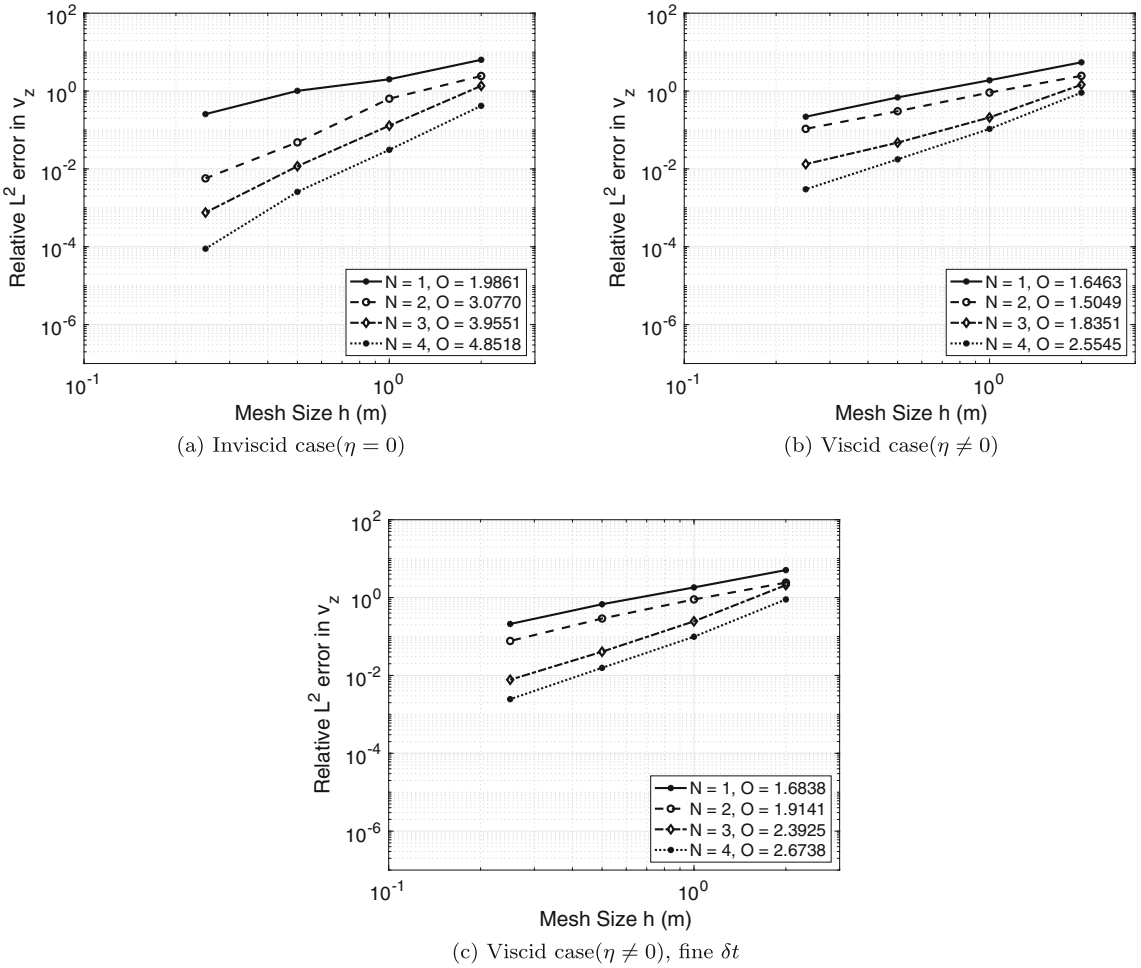

(a) Inviscid case($\eta = 0$)

(b) Viscid case($\eta \neq 0$)

(c) Viscid case($\eta \neq 0$), fine δt

Fig. 3 L^2 error of the solid particle velocity (v_z) (in a plane wave) as a function of the mesh size h computed at $N = 1,\ 2,\ 3,$ and 4 for **a** inviscid case $\eta = 0$, **b** viscid case $\eta \neq 0$, and **c** viscid case $\eta \neq 0$ with very fine Δt

fluid pressure, computed at 22 Hz for an inviscid case ($\eta = 0$). We have used a polynomial degree $N = 4$. Table 1 shows the material properties of the poroacoustic medium used, an acoustic version of a brine-saturated sandstone. Figure 2a and b show a good agreement between solutions with an L^2 error of 0.04%. Figure 2c and d represent a comparison between the solutions of the bulk and the fluid pressure, computed at 22 Hz for a viscid case ($\eta \neq 0$). Figure 2c and d show a good agreement with an L^2 error of 0.05%.

5.2 Poroelastic medium: convergence test

An analytical solution for plane waves of the poroelastic system (25) is given by [11] and [13]. We implemented the solution computed by de la Puente et al. [13] to test the convergence of the numerical scheme in (57). The convergence analysis is performed in both regimes, non-stiff and stiff, with a periodic boundary condition. The convergence is computed for brine-filled (viscid and inviscid) isotropic sandstone. The properties are given in

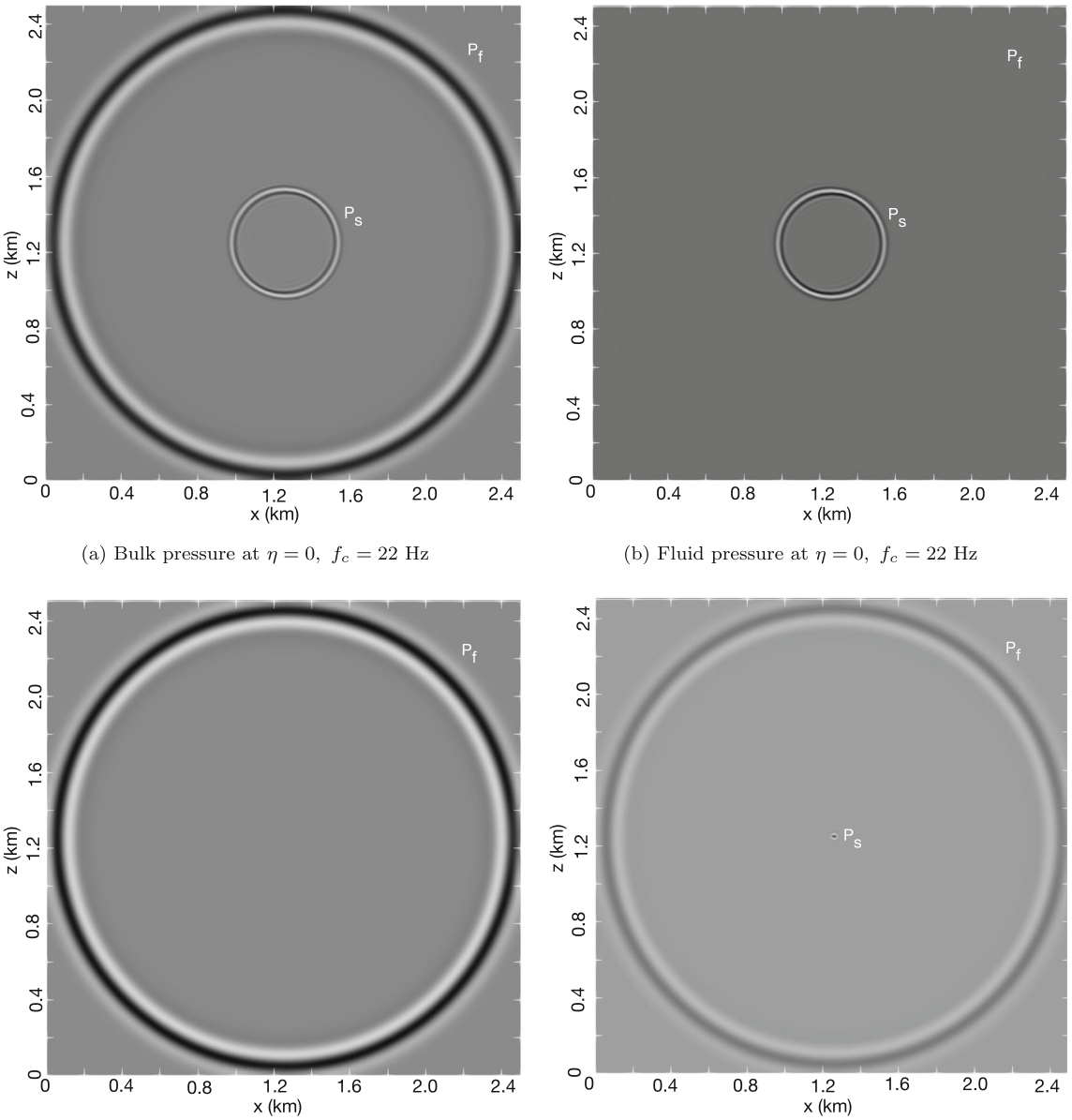

(a) Bulk pressure at $\eta = 0,\ f_c = 22$ Hz

(b) Fluid pressure at $\eta = 0,\ f_c = 22$ Hz

(c) Bulk pressure at $\eta \neq 0,\ f_c = 22$ Hz

(d) Fluid pressure at $\eta \neq 0,\ f_c = 22$ Hz

Fig. 4 Snapshots of **a** bulk pressure p **b** fluid pressure p_f for the inviscid case ($\eta = 0$), computed at $t = 0.36$ s. Snapshots of **c** bulk pressure p **d** fluid pressure for viscid case ($\eta \neq 0$), computed at $t = 0.36$ s. The forcing function is a bulk source (energy is partitioned between solid and fluid) with a central frequency of 22 Hz. Numerical solution is computed for a polynomial of order 4. P_f: Fast compressional wave, P_s: slow wave (Biot mode)

Table 2. The CFL value is 0.4 for the computation. Figure 3a shows a convergence plot of the L^2 error of v_z in the non-stiff regime. The rate of convergence shows an order of $O(h^{N+1})$. Figure 3b represents the convergence plot of the L^2 error of v_z in the stiff regime. The convergence reported in Fig. 3 are the minimum rate of convergence. It is worth to note that the rate of convergence deteriorates due to the fact that operator splitting is a first-order accurate in time. For $N = 1$, the rate of convergence is ≈ 2, which is expected rate for a nodal DG scheme. For higher orders ($N = 2,\ 3,\ 4$) the convergence rate is dominated by the accuracy of the time integration scheme. We also performed the convergence rate for a very fine time step (Δt), presented in Fig. 3c, so that the operator splitting approach does not destroy the h convergence rate of the DG operator. Though, the minimum convergence rate improves over those in Fig. 3b but it makes the computation very slow. The operator splitting approach will not provide a very high accuracy as the operators associated with the non-stiff system $[\nabla \cdot \mathcal{A}]$ and stiff system (**D**) do not commute. Thus, it is imperative to suggest that the reasonable time step for the computation will be the maximum Δt allowed by the

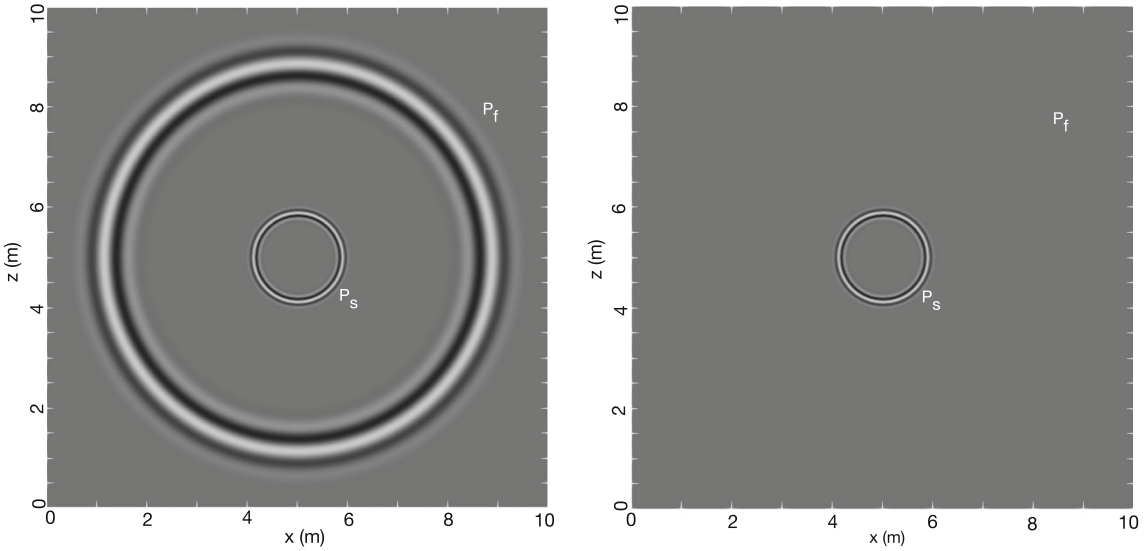

(a) Bulk pressure at $\eta = 0,\ f_c = 4.5$ kHz

(b) Fluid pressure at $\eta = 0,\ f_c = 4.5$ kHz

(c) Bulk pressure at $\eta \neq 0,\ f_c = 4.5$ kHz

(d) Fluid pressure at $\eta \neq 0,\ f_c = 4.5$ kHz

Fig. 5 Snapshots of **a** bulk pressure p **b** fluid pressure p_f for the inviscid case ($\eta = 0$), computed at $t = 1.2$ ms. Snapshots of **c** bulk pressure p **d** fluid pressure for viscid case ($\eta \neq 0$), computed at $t = 1.2$ ms. The forcing function is bulk source (energy is partitioned between solid and fluid) with a central frequency of 22 Hz. Numerical solution is computed for a polynomial of order 4. P_f: Fast compressional wave, P_s: slow wave (Biot mode)

standard nodal DG scheme for the non-stiff case. However, in any case, the convergence rate is better than any low-order scheme.

5.3 Homogeneous poroacoustic medium: wave-field simulation

We use the properties of the poroacoustic medium described in Table 1, which represents a brine-saturated sandstone. The Biot's characteristic frequency for this medium is 18 kHz. Thus, the system of Eq. (25) and the numerical scheme (57) used in this work is valid for a frequency of the forcing function (**f**) less than 18 kHz. We have performed the simulations for the inviscid ($\eta = 0$) and viscid ($\eta \neq 0$) cases at frequencies varying from the seismic to the sonic range. The forcing function considered here is given in (61) and located at the center of the computational domain.

Figure 4 shows the numerical results with a forcing function of central frequency ($f_c = 22$ Hz). The size of the computational domain is 2.5 km $\times$ 2.5 km. The minimum size of the edge of the equilateral triangles, used to mesh the domain, is 20 m. Figure 5a and b represent the snapshots of bulk and fluid pressures, respectively, computed at $t = 0.36$ s and $\eta = 0$ with a bulk forcing function. The bulk forcing function assumes that the energy is partitioned between the solid and fluid phases [8]. Figure 4a clearly shows both phases of P waves (fast and slow) whereas the fluid pressure in Fig. 4b is dominated by a slow P wave, being the amplitude of the fast P wave very subtle. Since the results in Fig. 4a and b are simulated for the inviscid case, the slow P wave is not attenuated. Figure 4c and d represents the bulk and fluid pressures at $t = 0.36$ s and $\eta \neq 0$. We remark that the slow P wave in Fig. 4c and d attenuates faster than those in Fig. 4a and b. This is in agreement with the physics of Biot's theory, which states that for

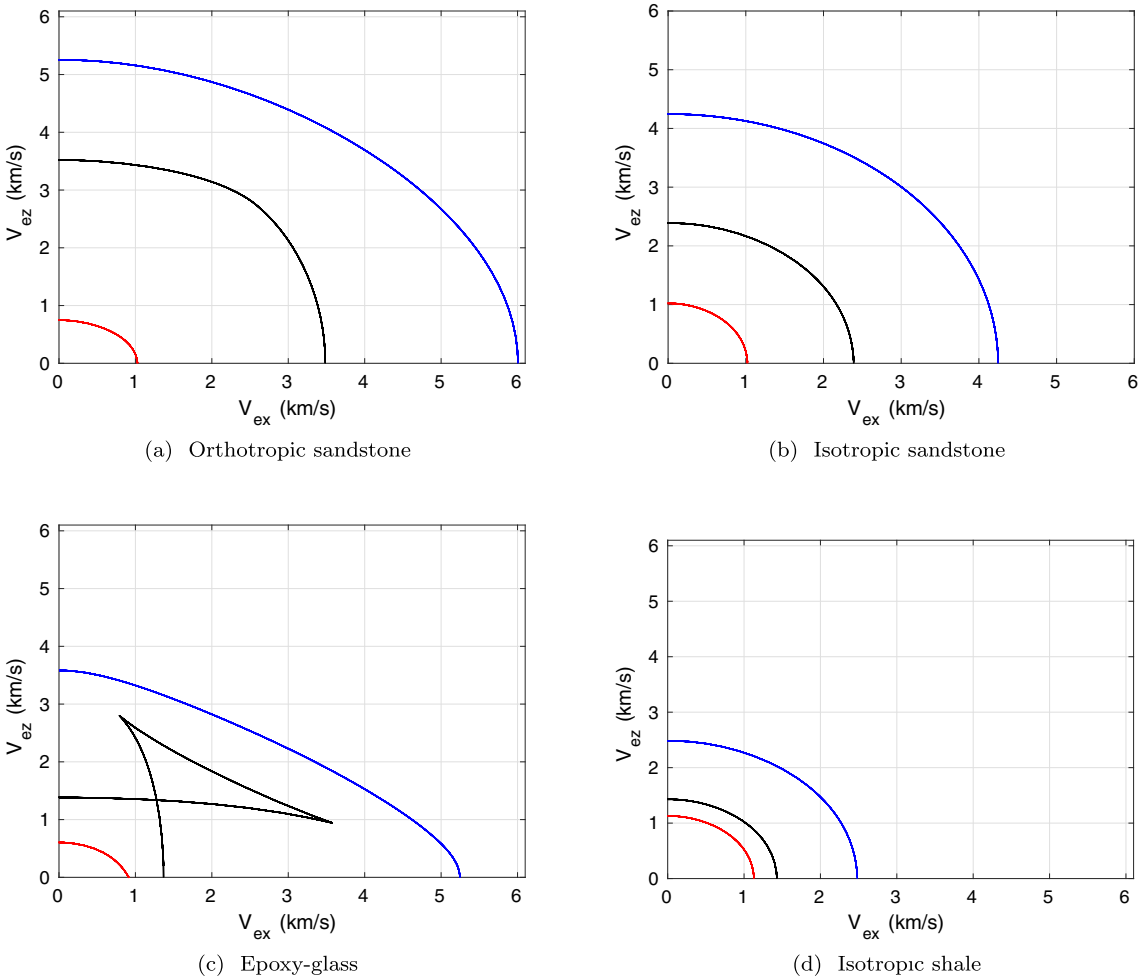

(a) Orthotropic sandstone

(b) Isotropic sandstone

(c) Epoxy-glass

(d) Isotropic shale

Fig. 6 Energy velocity surface for $\eta = 0$, computed in a $x - z$ plane for **a** orthotropic sandstone, **b** isotropic sandstone, **c** epoxy-glass and **d** isotropic shale. The material properties are given in Table 2. For homogenous media, the geometry of the energy velocity surfaces resembles the wavefronts of the compressional, shear, and slow P waves. V_{ex} and V_{ez} are energy velocities in $x-$ and $z-$ directions, respectively

$\omega \leq \omega_c$, the slow P wave becomes a diffusive mode due to the dominance of viscous forces over the inertial forces.

Figure 5 shows the numerical results for the same poroacoustic medium but with a forcing function of central frequency ($f_c = 4.5$ kHz). The size of the computational domain in this case is 10 m × 10 m. The minimum size of the mesh is 0.04 m. Figure 5a and b represent the snapshots of the bulk and fluid pressures, respectively, computed at $t = 1.2$ ms and $\eta = 0$ with a bulk forcing function. Figure 5c and d are the bulk and fluid pressures, respectively, computed for a bulk forcing function at $t = 1.2$ ms and $\eta \neq 0$. The physical interpretation of Fig. 5 is the same as that of the Fig. 4, just at a different scale and the slow P wave propagates faster than those seen in Fig. 4. The dispersion analysis also shows a non-zero velocity of the slow P wave at frequency 4.5 kHz [8].

5.4 Homogeneous poroelastic medium: wave-field simulation

Here, we illustrate the effect of anisotropy in (25) using our numerical scheme. We have considered, sandstone (orthotropic and isotropic), epoxy-glass and shale, brine filled, with the material properties given in Table 2. In

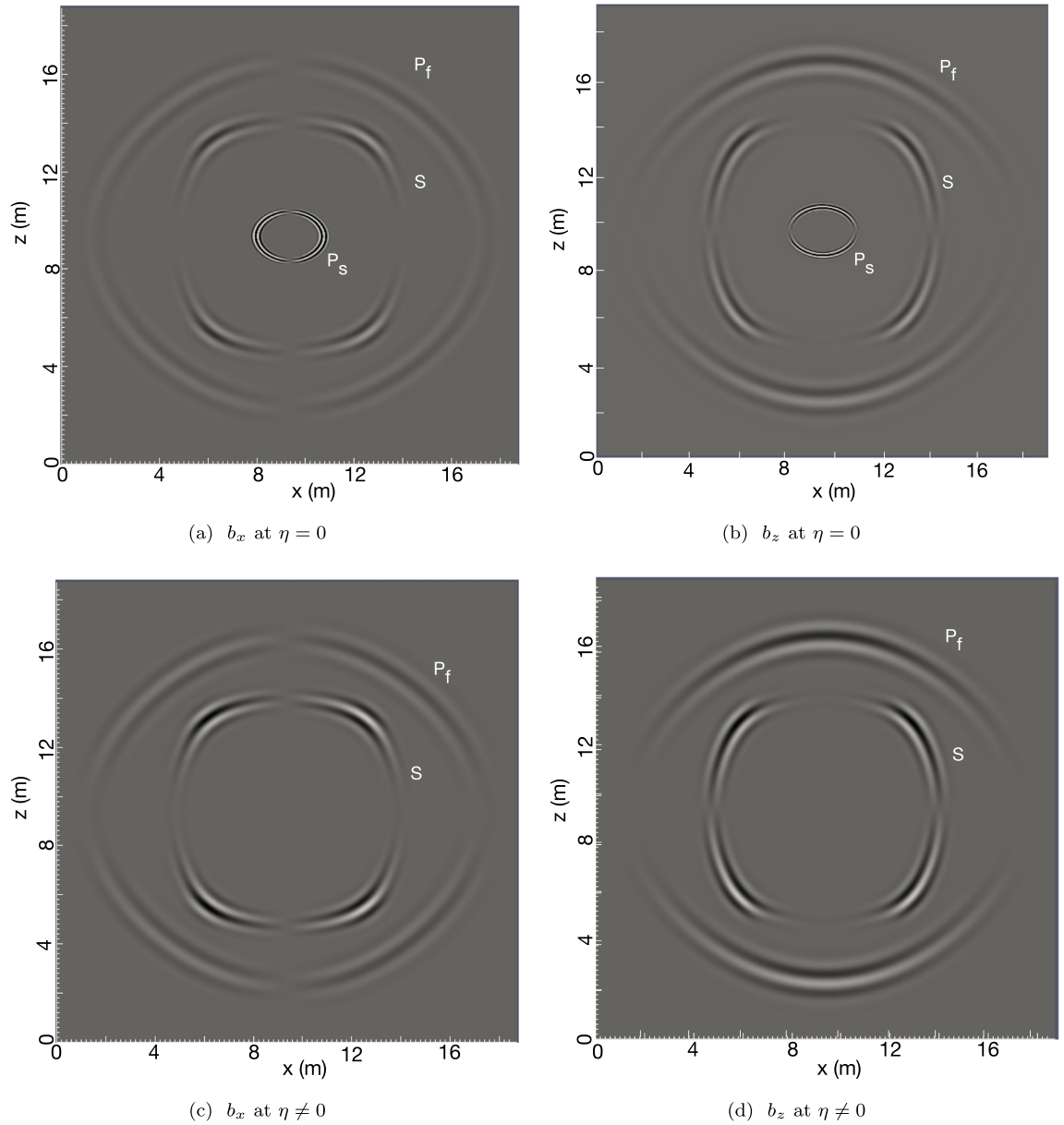

(a) b_x at $\eta = 0$

(b) b_z at $\eta = 0$

(c) b_x at $\eta \neq 0$

(d) b_z at $\eta \neq 0$

Fig. 7 Snapshots of the center of mass particle velocity in orthotropic sandstone, computed at $t = 1.6$ ms, where **a** and **b** corresponds to $\eta = 0$, and **c** and **d** corresponds to $\eta \neq 0$. The central frequency of the forcing function is 3730 Hz. The solution is computed for a polynomial of order 4. P_f: Fast compressional wave, S: Shear wave, P_s: slow wave (Biot mode)

order to have a detailed insight into the results of a poroelastic simulation, the energy velocity surfaces are computed for the materials with properties described in Table 2, solving the eigenvalue problem expressed in (73) in Appendix B. The surfaces include fast compressional, shear, and slow compressional waves with respect to azimuth. Figure 6a, b, c, and d show the energy velocities of the orthotropic sandstone, isotropic sandstone, epoxy-glass, and shale, respectively. The geometry of the energy velocity surface always agrees with the trajectory of the advancing wavefronts of the modes.

We have carried out numerical simulations with our scheme in order to compare with the energy velocity surfaces. In the subsequent discussions the field represents the center of mass particle velocity vector [30], which is expressed as

$$\mathbf{b} = \mathbf{v} + \left(\frac{\rho_f}{\rho}\right)\mathbf{q}. \tag{62}$$

The forcing function, in the subsequent simulation is given in (61) with a non-zero force corresponding to a

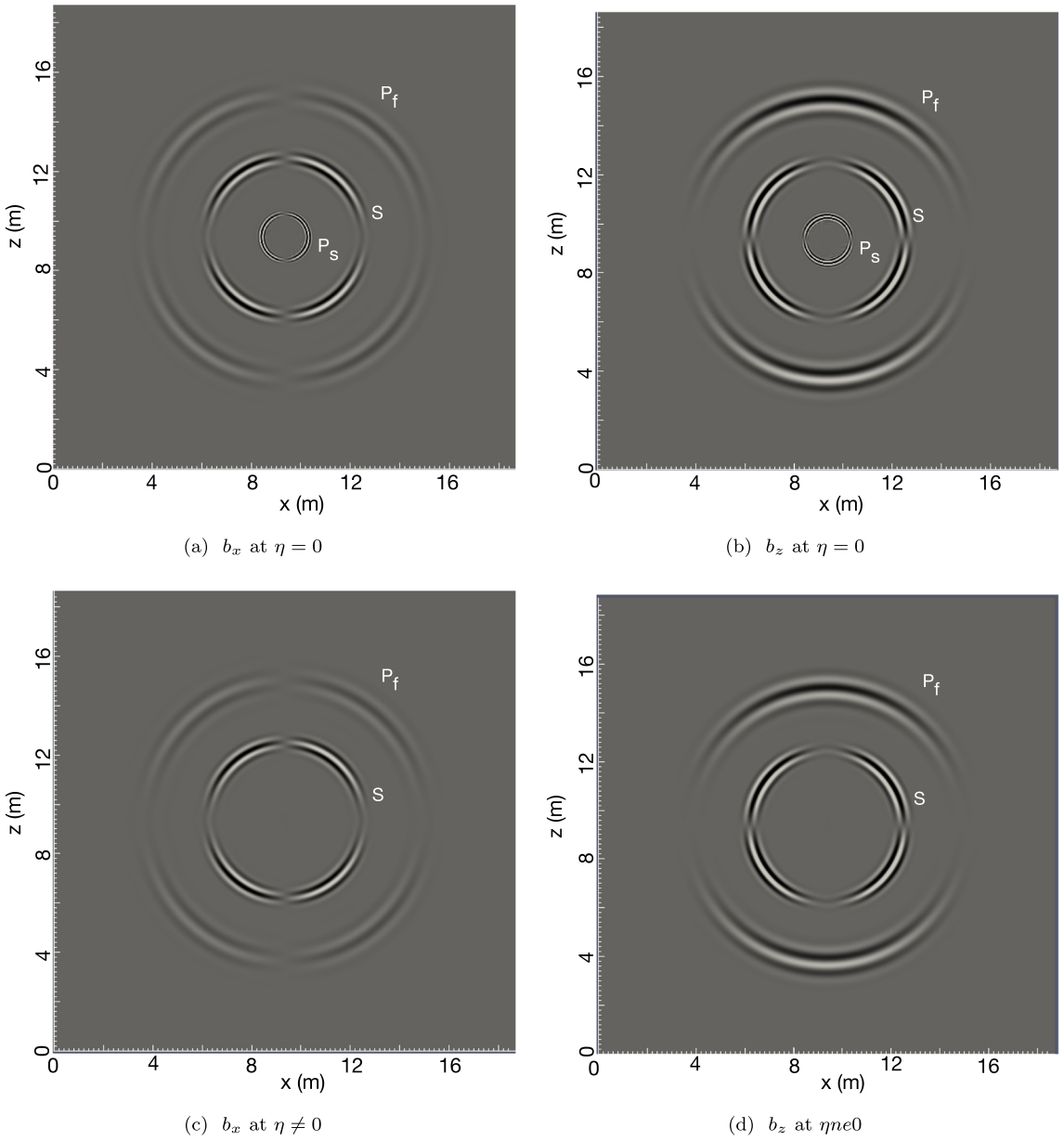

(a) b_x at $\eta = 0$

(b) b_z at $\eta = 0$

(c) b_x at $\eta \neq 0$

(d) b_z at $\eta ne 0$

Fig. 8 Snapshots of the center of mass particle velocity in isotropic sandstone, computed at $t = 2.2$ ms, where **a** and **b** corresponds to $\eta = 0$, and **c** and **d** corresponds to $\eta \neq 0$. The central frequency of the forcing function is 3730 Hz. The solution is computed for a polynomial of order 4. P_f: Fast compressional wave, S: Shear wave, P_s: slow wave (Biot mode)

vertical stress σ_{zz} and a fluid pressure p. The size of the computational domain is 18.25 m × 18.25 m. The minimum edge length is 5 cm.

Figure 7a–d represents the x and z components of the center of mass particle velocity of the orthotropic sandstone, where a and b correspond to the inviscid case ($\eta = 0$), and c and d to the viscid case ($\eta = 0$). The central frequency of the forcing function is $f_c = 3730$ Hz, and the basis functions have a polynomial degree $N = 4$. The propagation time is 1.6 ms. Three events can be clearly observed: the fast P mode (P_f, outer wavefront), the shear wave (S, middle wavefront), and the slow P mode (P_s, inner wavefront). In the viscid case, the slow mode diffuses faster and the medium behaves almost as a single phase medium.

Figure 8a–d show the $x-$ and $z-$ components of the center of mass particle velocity in an isotropic sandstone, where a and b correspond to the inviscid case ($\eta = 0$), and c and d to the viscid case ($\eta = 0$). Figure 8 is produced with the same simulation parameters as those in Fig. 7 except that the propagation time is 2.2 ms. The physical significance of Fig. 8 is the same as in Fig. 7 except the fact that the

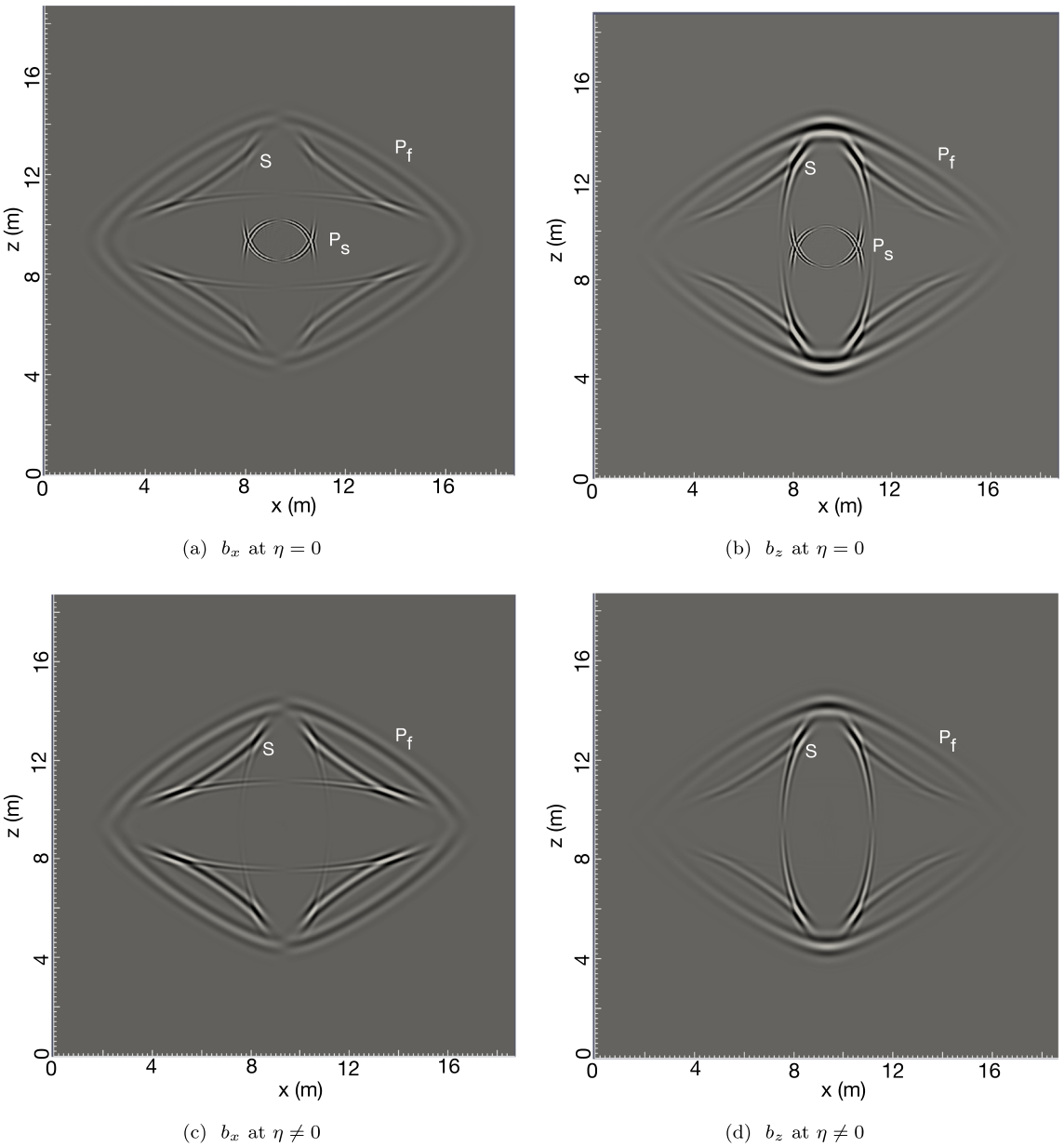

(a) b_x at $\eta = 0$

(b) b_z at $\eta = 0$

(c) b_x at $\eta \neq 0$

(d) b_z at $\eta \neq 0$

Fig. 9 Snapshots of the center of mass particle velocity in epoxy-glass, computed at $t = 1.8$ ms, where **a** and **b** corresponds to $\eta = 0$, and **c** and **d** corresponds to $\eta \neq 0$. The central frequency of the forcing function is 3730 Hz. The solution is computed for a polynomial of order 4. P_f: Fast compressional wave, S: Shear wave, P_s: slow wave (Biot mode)

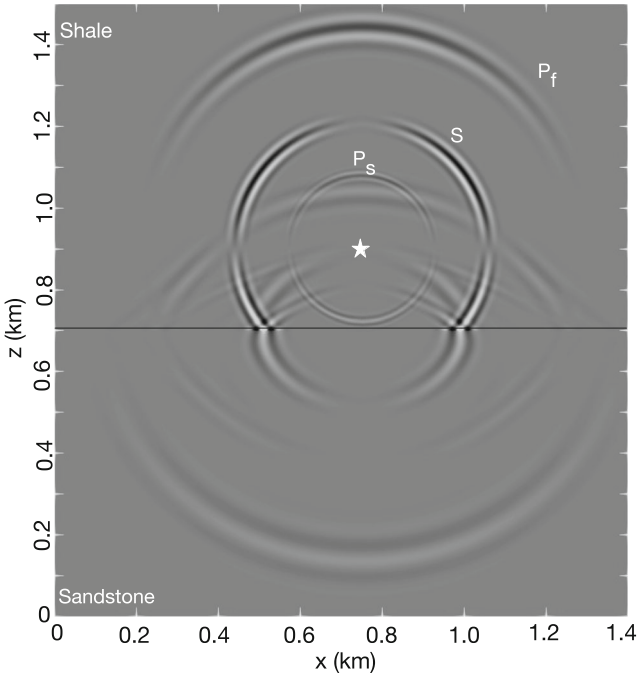

Fig. 10 Snapshot of the z-component of the center of mass particle velocity in an inviscid ($\eta = 0$) heterogenous medium, computed at $t = 0.25$ s .The central frequency of the forcing function is 45 Hz. The solution is computed for a polynomial of order 4. The star represents the location of the point source perturbation. P_f: Direct fast compressional wave, S: Direct shear wave, P_s: Direct slow wave (Biot mode)

radiation pattern is azimuthally invariant. The trajectory of the wavefronts mimics the surfaces of the energy velocity presented in Fig. 6b.

Snapshots of the $x-$ and $z-$ components of the center of mass particle velocity in the epoxy-glass porous medium are represented in Fig. 9. Figure 9a and b correspond to the inviscid case ($\eta = 0$), and c and d to the viscid case ($\eta = 0$). The central frequency is $f_c = 3135$ Hz. The propagation time is 1.9 ms. It is worth noting the cuspidal triangles of S and P_s which is a typical phenomena in anisotropic materials. At 45°, the polarization of the P_s mode wave is almost horizontal, which confirms the results shown in Fig. 3b of [9].

5.5 Heterogenous poroelastic medium: wave-field simulation

With this last example, we illustrate the effect of an interface between two porous media. A two-layer model comprising shale and sandstone, both of them filled with brine, is constructed. The size of the computational domain is 1400 m × 1500 m in the x and z directions, respectively. The minimum size of the edge of the triangular element, used to triangulate the domain, is 8 m. The forcing function is located at (750 m, 900 m) The propagation time is 0.25 s. A snapshot of the z component of the center of mass particle velocity is represented in Fig. 10 for an inviscid case ($\eta = 0$). Figure 10 clearly shows the direct, reflected, and transmitted wavefronts, corresponding to all three modes. The slow P wave is more prominent in the shale.

To justify the choice of the flux, a comparison between the solutions, obtained from using the Lax-Friedrich flux and the local Lax-Friedrich flux, is presented in Fig. 11. In the local Lax-Friedrich flux the λ [in (57)] is selected locally and thus resulting into a less dissipative scheme. The λ for local Lax-Friedrich is computed as

$$\lambda = \max\left(\lambda^-, \lambda^+\right). \tag{63}$$

Figure 11a and b show the comparison of solutions and residuals for b_x and b_z respectively, obtained from the Lax-Friedrich and the local Lax-Friedrich flux. The model

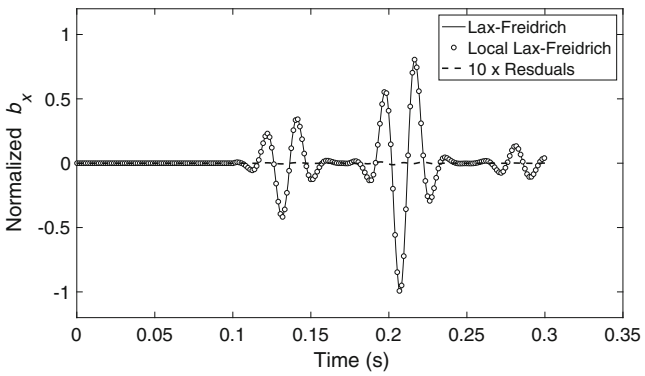

(a) Time-history of b_x

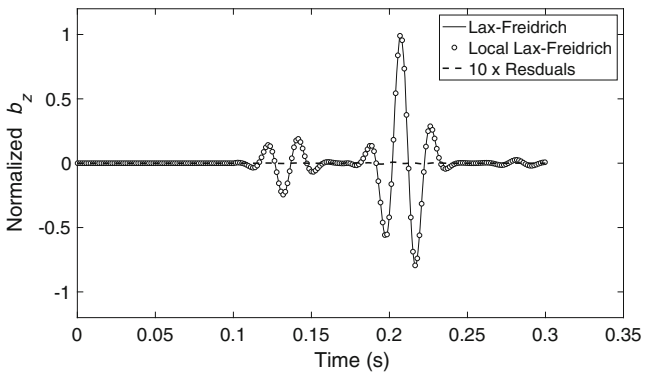

(b) Time-history of b_z

Fig. 11 A comparison between numerical solutions obtained from Lax-Friedrich and local Lax-Friedrich flux, where **a** and **b** correspond to x and z components of normalized center of mass particle velocity. The time history of the solution is recovered at receiver located in model, same as in Fig. 10, with coordinates $(x, z) = (900\text{ m}, 1100\text{ m})$. The residual between the solutions is magnified by the factor of 10

and material parmeters, used to compute the solutions in Fig. 11, are same as that in Fig. 10. The time history of the solution is retrieved at a node with $(x, z) =$ (900 m, 1100 m). The residuals plot in Fig. 11, magnified by a factor of ten, clearly shows that the choice of the flux does not make a significant difference. As a matter of fact, Cockburn and Shu [6] have also shown that the choice of the flux is not important for higer-order simulations, as long as the scheme is stable. This indicates that as the order of a simulation increases, the choice of numerical flux becomes less significant. This view has lead to the simple and dissipative Lax-Friedrich (LF) flux being used within many DG methods. Furthermore, The findings of Cockburn and Shu [6] are also substantiated by Wheatley et al. [34] for a Magneto-hydrodynamic system.

6 Discussion

We have developed a nodal DG-method-based approach to simulate poroelastic wave phenomena and demonstrated its ability to generate correct solutions in both homogeneous and heterogeneous domains. We use the Lax-Friedrich flux, which extends from isotropic to anisotropic media naturally, unlike the upwind flux used in [33]. The poroelastic system has very complex Jacobian matrices, which pose a computational challenge for the eigen-decomposition. Thus, the computation of the exact flux with such a complex wave structure will be very expensive. The Lax-Friedrich flux is slightly more dissipative than the upwind flux but the effects of numerical dissipation is less prominent at high order [12, 21]. We also compared the solutions obtained from global and local Lax-Friedrich flux and showed that the choice of flux does not have significant effects on the high-order simulations [6, 34].

Another challenge is to circumvent the effect of the stiffness, caused by strong dissipation at low frequencies. In the present work, we address the stiffness by using a first-order operator splitting approach. This operator deteriorates the convergence rate for a viscid case. We find that it works reasonably well for all spatial orders tested, i.e., $N = 1..4$. Existing alternatives, include [13] who use a locally implicit time integration scheme. Our scheme is simpler but fully explicit.

7 Conclusions

We have proved the well-posedness of the poroelastic system by showing that the energy rate in the system is bounded. We also have proposed a numerical scheme in strong form based on the nodal discontinuous Galerkin finite-element method, paired with a first-order operator splitting approach to handle the stiffness present in the system. We have proved the accuracy of the proposed scheme by comparing the numerical solution with an analytical solution. A convergence study shows $O(h^{N+1})$ accuracy. We have further simulated the wave fields for various real-case scenarios comprising homogenous and heterogeneous materials with anisotropy. The simulation correctly produces the fast and slow compressional waves along with the shear waves.

Acknowledgements KS would like to acknowledge the School of Geology, OSU and the MCSS, EPFL Switzerland, for providing the fund to carry out this work. We also acknowledge the OGS, Italy for hosting KS at various occasions. We thank editors and three anonymous reviewers for very useful comments. KS would like to acknowledge Sundeep Sharma at Devon Energy, for various discussions and proof-reading the manuscript. This is Boone Pickens School of Geology, Oklahoma State University, contribution number 2019-100.

Appendix A: Solution of the stiff part

The system of equations represented by (47) is expressed as

$$\partial_t v_x = -\frac{\eta}{\kappa_1}\beta_{12}^{(1)} q_x, \tag{64}$$

$$\partial_t v_z = -\frac{\eta}{\kappa_3}\beta_{12}^{(3)} q_z, \tag{65}$$

$$\partial_t q_x = -\frac{\eta}{\kappa_1}\beta_{22}^{(1)} q_x, \tag{66}$$

$$\partial_t q_z = -\frac{\eta}{\kappa_3}\beta_{22}^{(3)} q_z. \tag{67}$$

The solution of Eqs. (64)–(67) is given as

$$v_x = v_x^n + \frac{\beta_{12}^{(1)}}{\beta_{22}^{(1)}}[\exp\left(-\frac{\eta}{\kappa_1}\beta_{22}^{(1)} dt\right) - 1]q_x^n, \tag{68}$$

$$v_z = v_z^n + \frac{\beta_{12}^{(3)}}{\beta_{22}^{(3)}}[\exp\left(-\frac{\eta}{\kappa_3}\beta_{22}^{(3)} dt\right) - 1]q_z^n, \tag{69}$$

$$q_x = \exp\left(-\frac{\eta}{\kappa_1}\beta_{22}^{(1)} dt\right) q_x^n, \tag{70}$$

$$q_z = \exp\left(-\frac{\eta}{\kappa_3}\beta_{22}^{(3)} dt\right) q_z^n. \tag{71}$$

Appendix B: Computation of λ in (57)

A plane-wave solution for the particle velocity vector $V = [v_x, v_z, q_z, q_z]^T$ is

$$\mathbf{V} = \mathbf{V_0}\exp[\mathrm{i}(\mathbf{k}.\mathbf{x} - \omega t)], \tag{72}$$

where $\mathbf{V_0}$ is a constant complex vector and $\mathbf{k}$ is wave vector. Substituting (72) in (1)–(4) and (20)–(23) , we recover

$$\left(\mathbf{\Gamma}^{-1} \cdot \mathbf{L} \cdot \mathbf{C} - V\mathbf{I_4}\right).\mathbf{V} = 0, \tag{73}$$

where

$$\mathbf{\Gamma} = \begin{bmatrix} \rho & 0 & \rho_f & 0 \\ 0 & \rho & 0 & \rho_f \\ \rho_f & 0 & \mathrm{i}Y_1(-\omega)/\omega & 0 \\ 0 & \rho_f & 0 & \mathrm{i}Y_3(-\omega)/\omega \end{bmatrix},$$

$$\mathbf{L} = \begin{bmatrix} l_x & 0 & l_z & 0 \\ 0 & l_z & l_x & 0 \\ 0 & 0 & 0 & l_x \\ 0 & 0 & 0 & l_z \end{bmatrix}$$

$$\mathbf{C} = \begin{bmatrix} l_x c^u_{11} & l_z c^u_{13} & \alpha_1 M l_x & \alpha_1 M l_z \\ l_x c^u_{13} & l_z c^u_{33} & \alpha_3 M l_x & \alpha_3 M l_z \\ l_z c^u_{55} & l_x c^u_{55} & 0 & 0 \\ \alpha_1 M l_x & \alpha_3 M l_z & M l_x & M l_z \end{bmatrix},$$

with $Y_i(\omega) = \mathrm{i}\omega m_i + \eta/\kappa_i$ and l_x and l_z being direction cosines and $V = \frac{\omega^2}{k^2}$.

Term $\mathbf{V}$ in (73) represents the phase velocity of waves and can be computed by adopting the approach for eigenvalue computation. Thus

$$\lambda_i = (\mathrm{Re}(1/V_i)) \quad \text{for } i = 1...4,$$
$$\text{and} \quad \lambda = \max(\lambda_i)$$

Energy velocity $\mathbf{V_e}$ can be computed from

$$\mathbf{k^T} \cdot \mathbf{V_e} = \mathbf{V}. \tag{74}$$

Appendix C: System of poroacoustic wave equation

This system is

$$\partial_t \mathbf{q_p} + \mathbf{A_{1p}}\partial_x \mathbf{q_p} + \mathbf{B_{1p}}\partial_x \mathbf{q_p} = \mathbf{D_{1p}}\mathbf{q_p} + \mathbf{f_p}, \tag{75}$$

where

$$\mathbf{q_p} = [v_x \; v_z \; q_x \; q_z \; p \; p_f]^T,$$

with p being the bulk pressure, p_f is fluid pressure, v'^s and q'^s are solid and fluid particle velocity (relative to solid). $\mathbf{A_{1p}}$, $\mathbf{B_{1p}}$, and $\mathbf{D_{1p}}$ are defined as

$$\mathbf{A_{1p}} = -\begin{bmatrix} 0 & 0 & 0 & 0 & \beta_{11} & \beta_{12} \\ 0 & 0 & 0 & 0 & 0 & 0 \\ 0 & 0 & 0 & 0 & -\beta_{21} & -\beta_{22} \\ 0 & 0 & 0 & 0 & 0 & 0 \\ -H & 0 & -C & 0 & 0 & 0 \\ -C & 0 & -M & 0 & 0 & 0 \end{bmatrix},$$

$$\mathbf{B_{1p}} = -\begin{bmatrix} 0 & 0 & 0 & 0 & 0 & 0 \\ 0 & 0 & 0 & 0 & \beta_{11} & \beta_{12} \\ 0 & 0 & 0 & 0 & 0 & 0 \\ 0 & 0 & 0 & 0 & -\beta_{21} & -\beta_{22} \\ 0 & -H & 0 & -C & 0 & 0 \\ 0 & -C & 0 & -M & 0 & 0 \end{bmatrix},$$

$$\mathbf{D_{1p}} = -\begin{bmatrix} 0 & 0 & \frac{\eta}{\kappa}\beta_{12} & 0 & 0 & 0 \\ 0 & 0 & 0 & \frac{\eta}{\kappa}\beta_{12} & 0 & 0 \\ 0 & 0 & -\frac{\eta}{\kappa}\beta_{22} & 0 & 0 & 0 \\ 0 & 0 & 0 & -\frac{\eta}{\kappa}\beta_{22} & 0 & 0 \\ 0 & 0 & 0 & 0 & 0 & 0 \\ 0 & 0 & 0 & 0 & 0 & 0 \end{bmatrix},$$

where β's, H, C, and M are dependent on the solid bulk modulus (K_s), the fluid bulk modulus (K_f), the solid density (ρ_s), the porosity (ϕ), the permeability (κ), the fluid density (ρ_f), and the viscosity (η) of the medium, elaborately expressed in [8].

References

1. Allard, J., Atalla, N.: Propagation of sound in porous media: Modelling Sound Absorbing Materials. Wiley, Hoboken (2009)
2. Badiey, M., Jaya, I., Cheng, A.H.: Propagator matrix for plane wave reflection from inhomogeneous anisotropic poroelastic seafloor. J. Comput. Acoust. **2**, 11–27 (1994)
3. Biot, M.A.: Theory of propagation of elastic waves in a fluid-saturated porous solid: I. Low frequency range. J. Acoust. Soc. Am. **28**, 168–178 (1956)
4. Biot, M.A.: Theory of propagation of elastic waves in a fluid-saturated porous solid: II. Higher frequency range. J. Acoust. Soc. Am. **28**, 179–191 (1956)
5. Biot, M.A.: Mechanics of deformation and acoustic propagation in porous media. J. Appl. Phys. **33**, 1482–1498 (1962)
6. Cockburn, B., Shu, C.W.: Runge–kutta discontinuous Galerkin methods for convection-dominated problems. J. Sci. Comput. **16**, 173–261 (2001)
7. Coussy, O., Zinszner, B.: Acoustics of porous media. Editions Technip (1987)
8. Carcione, J.M., Quiroga-Goode, G.: Some aspects of the physics and numerical modeling of Biot compressional waves. J. Comput. Acoust. **3**, 261–280 (1995)

9. Carcione, J.M.: Wave propagation in anisotropic, saturated porous media: Plane-wave theory and numerical simulation. J. Acoust. Soc. Am. **99**, 2655–2666 (1996)
10. Carcione, J.M., Morency, C., Santos, J.E.: Computational poroelasticity—A review. Geophysics **75**, 229–243 (2010)
11. Carcione, J.M. Wave Fields in Real Media: Theory and Numerical Simulation of Wave Propagation in Anisotropic, Anelastic, Porous and Electromagnetic Media, 3rd edn. Elsevier Science, New York City (2014)
12. de la Puente, J., Käser, M., Dumbser, M., Igel, H.: An arbitrary high-order discontinuous Galerkin method for elastic waves on unstructured meshes-IV. Anisotropy. Geophys. J. Int. **169**, 1210–1228 (2007)
13. de la Puente, J., Dumbser, M., Käser, M., Igel, H.: Discontinuous Galerkin methods for wave propagation in poroelastic media. Geophysics **73**(2008), 77–97 (2008)
14. Dablain, M.A.: The application of high-order differencing to the scalar wave equation. Geophysics **51**, 54–66 (1986)
15. Dai, N., Vafidis, A., Kanasewich, E.R.: Wave propagation in heterogeneous, porous media: a velocity-stress, finite-difference method. Geophysics **60**, 327–340 (1995)
16. Dumbser, M., Enaux, C., Toro, E.F.: Finite volume schemes of very high order of accuracy for stiff hyperbolic balance laws. J. Comput. Phys. **227**, 3971–4001 (2008)
17. Dupuy, B., De Barros, L., Garambois, S., Virieux, J.: Wave propagation in heterogeneous porous media formulated in the frequency-space domain using a discontinuous Galerkin method. Geophysics **76**(4), N13–N28 (2011)
18. Etgen, J.T., Dellinger, J.: Accurate wave-equation modeling. SEG Technical Program Expanded Abstracts, 494–497 (1989)
19. Garg, S.K., Nayfeh, A.H., Good, A.J.: Compressional waves in fluid-saturated elastic porous media. J. Appl. Phys. **45**, 1968–1974 (1974)
20. Grote, M.J., Schneebeli, A., Schötzau, D.: Discontinuous Galerkin finite element method for the wave equation. SIAM J. Numer. Anal. **44**(2006), 2408–2431 (2006)
21. Hesthaven, J.S., Warburton, T.: Nodal Discontinuous Galerkin Methods: Algorithms, Analysis, and Applications. Springer Science & Business Media, Berlin (2007)
22. Hunter, R.J.: Foundations of Colloid Science. Oxford University Press, Oxford (2001)
23. Käser, M., Dumbser, M., De La Puente, J., Igel, H.: An arbitrary high-order discontinuous Galerkin method for elastic waves on unstructured meshes—III. Viscoelastic attenuation. Geophys. J. Int. **168**, 224–242 (2007)
24. Komatitsch, D., Vilotte, J.P.: The spectral element method: an efficient tool to simulate the seismic response of 2D and 3D geological structures. Bull. Seismol. Soc. Am. **88**, 368–392 (1998)
25. Lemoine, G.I., Ou, M.Y., LeVeque, R.J.: High-resolution finite volume modeling of wave propagation in orthotropic poroelastic media. SIAM J. Sci. Comput. **35**, 176–206 (2013)
26. Levander, A.R.: Fourth-order finite-difference p-SV seismograms. Geophysics **53**, 1425–1436 (1988)
27. LeVeque, R.J.: Finite Volume Methods for Hyperbolic problems. Cambridge University Press, Cambridge (2002)
28. Özdenvar, T., McMechan, G.A.: Algorithms for staggered-grid computations for poroelastic, elastic, acoustic, and scalar wave equations. Geophys. Prospect. **45**, 403–420 (1997)
29. Pride, S.R.: Relationships between seismic and hydrological properties. Hydrogeophysics, 253–290 (2005)
30. Sahay, P.N.: Natural field variables in dynamic poroelasticity. SEG Technical Program Expanded Abstracts. Society of Exploration Geophysicists, 1163–1166 (1994)
31. Santos, J.E., Oreña, E.J.: Elastic wave propagation in fluid-saturated porous media- Part II The Galerkin procedures. Mathematical Modelling and Numerical Analysis **20**, 129–139 (1986)
32. Virieux, J.: P-SV wave propagation in heterogeneous media: Velocity-stress finite-difference method. Geophysics **51**, 889–901 (1986)
33. Ward, N.D., Lähivaara, T., Eveson, S.: A discontinuous Galerkin method for poroelastic wave propagation: The two-dimensional case. J. Comput. Phys. **350**(2017), 690-727 (2017)
34. Wheatley, V., Kumar, H., Huguenot, P.: On the role of Riemann solvers in discontinuous Galerkin methods for magnetohydrodynamics. J. Comput. Phys. **229**(3), 660–680 (2010)
35. Ye, R., de Hoop, M.V., Petrovitch, C.L., Pyrak-Nolte, L.J., Wilcox, L.C.: A discontinuous Galerkin method with a modified penalty flux for the propagation and scattering of acousto-elastic waves. Geophys. J. Int. **205**, 1267–1289 (2016)
36. Zeng, Y., He, J., Liu, Q.: The application of the perfectly matched layer in numerical modeling of wave propagation in poroelastic media. Geophysics **66**(4), 1258–1266 (2001)

Affiliations

Khemraj Shukla[1] · Jan S. Hesthaven[2] · José M. Carcione[3] · Ruichao Ye[4] · Josep de la Puente[5] · Priyank Jaiswal[1]

Jan S. Hesthaven
jan.hesthaven@epfl.ch

José M. Carcione
jcarcione@inogs.it

Ruichao Ye
ruichao.ye@gmail.com

Josep de la Puente
josep.delapuente@bsc.es

Priyank Jaiswal
priyank.jaiswal@okstate.edu

1 Oklahoma State University, Stillwater, OK, USA

2 MCSS, EPFL, Lausanne, Switzerland

3 Istituto Nazionale di Oceanografia e di Geofisica Sperimentale (OGS), Borgo Grotta Gigante 42c, 34010, Sgonico, Trieste Italy

4 Rice University, Houston, TX 77005, USA

5 Barcelona Supercomputing Center (BSC), Barcelona, Spain